

Residual Gas Effects on Detached Solidification in Microgravity

**Final Report
21 June 2000 to 30 November 2004**

NASA Grant NAG 8-1703

**International Center for Gravity Materials Science and Applications
Clarkson University
Potsdam NY 13699-5814**

Phone: 1-315-268-7672; <http://www.clarkson.edu/~regel/center.htm>

Principal Investigator: Professor William R. Wilcox
Department of Chemical Engineering
wilcox@clarkson.edu

Co-Investigator: Professor Liya L. Regel
Department of Electrical and Computer Engineering
regel@clarkson.edu

Graduate assistants: Suresh Ramakrishnan
Arun Kota
Gaurav Anand
Department of Chemical Engineering

Contents

Summary	2
1. Background and introduction	2
1.1. Detached solidification	2
1.2. Contact-angle measurements	6
References	7
2. Interaction of oxygen with molten Ga-doped InSb	10
2.1. Introduction	10
2.2. Experimental apparatus and methods	11
2.3. Experimental results	16
2.4. Discussion and Conclusions	22
References	25
3. Revised experimental methods	27
3.1. Experimental apparatus	27
3.3. Description of components	27
3.3.1. Split-tube furnace	27
3.3.2. Quartz cell	28
3.3.3. Gas system	28
3.3.4. Oxygen analyzer	29
3.4. Experimental methods	30
3.4.1. Changes in the apparatus	31
3.4.2. Experimental procedure	31
3.4.3. Data analysis	34
3.4.4. Contact angle determination using a polynomial fit near the contact point	40
References	43
4. Recent results on high-purity InSb	44
4.1. Polynomial technique to determine contact angle	44
4.1.1. Fitting function	44
4.1.2. Order of polynomial and the number of pixels used	45
4.1.3. Substrate plate tilt correction	46
References	47

SUMMARY

Our long term goal has been to make detached solidification reproducible, which requires a full understanding of the mechanisms underlying it. Our Moving Meniscus Model of steady-state detachment predicts that it depends strongly on the surface tension of the melt and the advancing contact angle with the ampoule wall. Thus, the objective of the current project was to determine the influence of residual gases on the surface tension and contact angle of molten semiconductors on typical ampoule materials. Our focus was on the influence of oxygen on indium antimonide on clean silica ("quartz").

The research was performed by three chemical engineering graduate students, the third of whom will complete his research in the summer of 2005.

Originally, we had planned to use a sealed silica cell containing a zirconia electrochemical element to control the oxygen partial pressure. However, zirconia requires an operating temperature above the 530°C melting point of InSb and is difficult to form a gas-tight seal with silica. Thus, we decided instead to flow an oxygen-containing gas through the cell. A special apparatus was designed, built and perfected. A piece of InSb was placed on a horizontal silica plate in a quartz cell. High purity argon, helium or hydrogen-containing gas is passed continuously through the cell while the oxygen concentration in the effluent gas is measured. The shape of the resulting drop was used to determine contact angle and surface tension of Ga-doped and high purity InSb. Oxygen appeared to decrease the contact angle, and definitely did not increase it.

The following section gives the background for the research. Section 2 summarizes the results obtained on Ga-doped InSb with relatively high oxygen concentrations. Section 3 describes recent improvements made to the apparatus and methods of analysis. Section 4 gives recent results for high-purity InSb at low oxygen concentrations. Final results will be obtained only this summer (2005). Each section has its own references.

1. BACKGROUND AND INTRODUCTION

1.1. Detached solidification

Detached solidification has been observed in many microgravity experiments [1].¹ When it occurred, the perfection of the resulting crystals was greatly increased, making them much more useful for electronic and opto-electronic devices. Although detachment has been common, it has also been non-reproducible and erratic, for unknown reasons. Our long term goal is to make detachment reproducible, which requires a full understanding of the mechanisms underlying it.

Detached solidification was first observed in Skylab experiments about 25 years ago. Our 1995 Moving Meniscus Model provided the first real understanding of the mechanism [2]. Schematic diagrams are given in Figures 1.1 and 2. We explored the consequences of this model for InSb

¹ Each section has its own references, each beginning anew with [1].

[3-9] and for water [10] using numerical solutions of the differential equations and boundary conditions for fluid flow and mass transfer of dissolved gas.

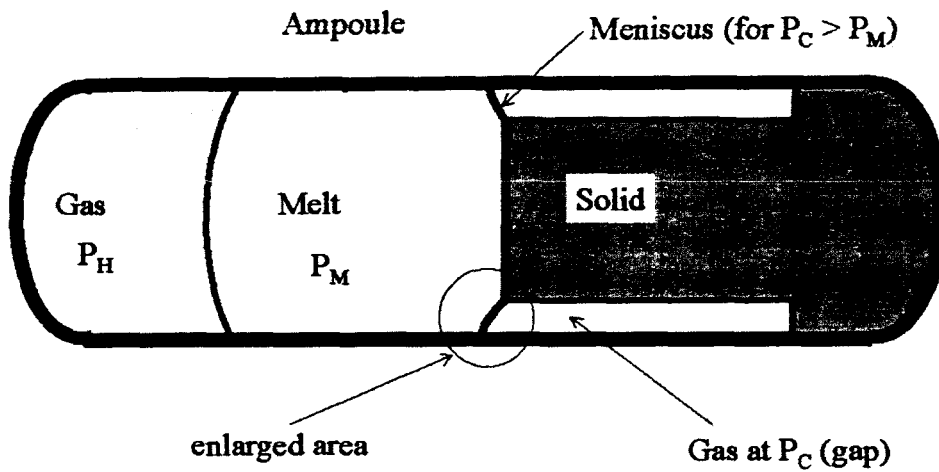


Figure 1.1. The Moving Meniscus Model of detached solidification [2-10].
The enlarged area is shown in Figure 2.

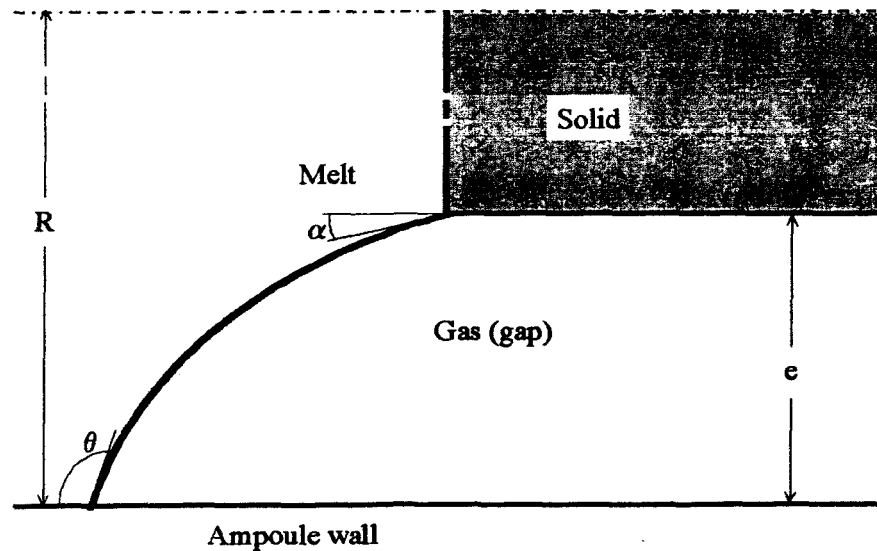


Figure 1.2. Enlarged meniscus area from Figure 1.1. As solidification progresses, the meniscus advances along the ampoule wall. Here α is the growth angle, θ is the contact angle, e is the gap width, and R is the ampoule diameter.

We showed that detachment is favored by a high contact angle² of the melt on the ampoule wall, high growth angle, low surface tension between the melt and the gas in the gap, high concentration of dissolved gas, and intermediate freezing rates.

Detached solidification of lightly gallium-doped indium antimonide was achieved in the laboratory only when the ampoule was coated with hexagonal boron nitride and when the material appeared to be oxide-free [43]. A furnace was constructed with the temperature increasing with height in order to minimize buoyancy-driven convection, so as to maximize transport of segregated dissolved gases into the gap between the growing solid and the ampoule wall. There appeared to be no difference in results with freezing rates of 5 mm/h and 10 mm/h. Best results were obtained when the ampoule was backfilled with 20 kPa of Ar-10% H_2 prior to sealing. The detached portions were depressed by several μm from adjacent attached regions, were dull, and sometimes had microfacets and steps.

A vertical Bridgman-Stockbarger apparatus was used to directionally solidify water upward, in the hope that detached solidification would evolve from gas bubbles forming on the wall [42]. A large contact angle of the water on the ampoule wall and a high solubility of the dissolved gas caused gas bubbles or tubes to form only at the ampoule wall, and not in the interior. Gas tubes were often nearly periodically spaced around the ampoule wall, with a spacing that increased with ampoule diameter and decreased with freezing rate. The width of the gas tubes was nearly independent of the ampoule diameter and freezing rate. A high degree of detachment was obtained with a rough, non-wetting coating on the ampoule wall, but full detachment was not achieved. This indicates that detachment does not occur by propagation of a single gas bubble around the periphery of the freezing interface. The convection near the freezing interface influenced gas bubble formation, and was outward for a concave freezing interface and inward for a convex interface. Similar semi-periodic gas tubes were produced in freezing of zone-refined naphthalene.

Non-dimensionalization of the governing equations for the Moving Meniscus Model allowed consolidation of the operating conditions and physical properties into five dimensionless parameters [41,44]. At steady state, the flux of gas dissolved in the melt moving toward the freezing interface must equal the sum of the flux of gas into the gap plus that being incorporated in the growing solid. Both numerical and material balance results give two solutions, with an extremum value of each variable beyond which steady detachment is impossible. This behavior is now understood to originate from satisfaction of the material balance at two different gap widths, with these two solutions becoming identical at an extremum condition beyond which the material balance cannot be satisfied. Only one solution is obtained when no gas is incorporated in the solid. In the presence of gravity, the gas pressure in the gap must be much larger to compensate for the added hydrostatic pressure, causing the gap width to be narrow.

Thus, residual gases play a major role in the Moving Meniscus Model, dissolving in the melt at the vapor end of the ampoule, and being expelled across a meniscus into the gap between the growing solid and the ampoule wall. Many uncertainties remain in this model, primarily because the behavior of the dissolved gases and their influence on the properties of the melt are unknown.

² A contact angle much less than 90° is generally said to characterize wetting behavior, while a non-wetting liquid would have a contact angle much greater than 90° . Non-wetting behavior favors detached solidification.

The objective of the present research proposed here was to clarify the role of oxygen in detached solidification.

Over the years it had been proposed that oxygen forms an oxide film, increases the contact angle of the melt on the ampoule wall, and avoids compositional inhomogeneities by stopping Marangoni convection arising from temperature and composition gradients along the meniscus. These remain speculative. For example, Duffar *et al.* [11] claimed that *"semiconductors can present very high contact angles on crucible materials, due to slight amounts of pollution by residual gases. This phenomena is used to explain the de-wetting of semiconductors observed when grown under microgravity conditions in smooth crucibles."* The basis for this conclusion is their observation made in sessile drop experiments with InSb on silica [12]. As described in [11], *"it was practically always necessary to shake the molten drops a little bit in order to measure the contact angle corresponding to thermodynamic equilibrium (112° in this particular case), otherwise contact angles as high as 170° might have been measured. This effect is attributed to absorption of some impurity at the surface of the drop which creates a layer subsequently removed when shaking. In any case this layer cannot be confused with a solid peel on the drops which were always perfectly clean and shiny before, during and after the experiments. The vacuum in the ampoules during sealing was below 10⁻⁷ mbar."* In other words, the authors attributed contact line pinning to the adsorption of impurities at the liquid-vapor interface. Furthermore, they assumed that this adsorption increased the contact angle. Numerous experiments with liquid metals on oxide surfaces have shown, however, that dissolved oxygen always lowers the contact angle [e.g., 13-15] for liquid metals. (Most molten semiconductors have metallic properties.) This behavior can be understood by examining the terms in the Young equation (without debating the merits or validity of this classical relationship):

$$\cos(\theta) = \frac{\sigma_{vs} - \sigma_{ls}}{\sigma_{lv}} \quad (1)$$

where θ is the contact angle, σ_{vs} is the surface energy between the vapor and the solid, σ_{lv} is the surface energy between melt and vapor, and σ_{ls} is the surface energy between melt and solid. The surface energy σ_{vs} between the vapor and the oxide solid should be relatively unaffected by the presence of trace amounts of oxygen. The surface tension σ_{lv} between liquid and vapor is lowered by oxygen adsorption on this surface, in accordance with the Gibbs relationship. The surface tension σ_{ls} tends to be strongly lowered by oxygen in the metal melt, due to chemical interactions with the solid [13]. One mechanism involves formation of O⁻² and positive metal ions that are attracted to the negatively charged oxygen atoms at the oxide surface. In some cases, a new oxide phase forms at the interface. Thus, both σ_{lv} and σ_{ls} are decreased, thereby increasing $\cos\theta$ and so decreasing the contact angle θ .

Another role sometimes attributed to oxygen in detached solidification is the suppression of convection driven by surface tension gradients along the meniscus. Although we have shown [3] that such Marangoni convection has little effect on the transport of gas into the gap, it would be expected to perturb the distribution of impurity dopant in the resulting crystals. Oxygen adsorption on the meniscus could explain why some crystals solidified with detachment exhibited no such perturbations while others did.

1.2. Contact-Angle Measurements

Many techniques were available for measurement of contact angles [16-21]. The sessile-drop technique shown in Figure 1.3 seemed most useful for liquid semiconductors because of the necessity to control the ambient gas surrounding the melt [22-29]. A solid piece of material is placed on a horizontal surface. The temperature is raised until a molten drop is formed. A photograph is taken from the side. The contact angle is obtained from the profile of the drop. When the drop is symmetric, software is available to fit the shape to theory such that values are obtained for both melt surface tension and contact angle. A simple protractor can be used when the drop is not symmetrical, to yield different values for the left and the right contact angles.

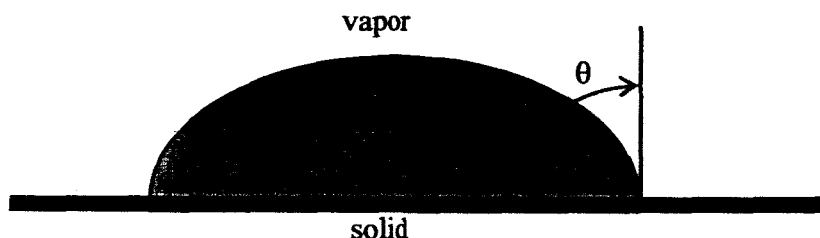


Figure 1.3. Schematic diagram of sessile drop technique.

One must distinguish between static and dynamic contact angles. The static contact angle is that measured when the contact line between vapor, melt and solid is stationary. Dynamic contact angles are those measured while the contact line moves. If the contact line is moving away from the melt, this is called the advancing contact angle. If the contact line is moving toward the melt (as in detached solidification), it is a retreating contact angle. The advancing contact angle tends to be greater than the static contact angle, while the retreating contact angle is smaller, with the values of both typically dependent on the rate of contact-line movement. In other words, movement of the contact line is inhibited. This sticking, and the resulting hysteresis when the direction is reversed, is usually attributed to heterogeneities in the solid surface [30-37]. All surfaces are heterogeneous on some scale, either due to variations in the surface elevation or to variations in surface composition.

In the sessile drop technique, an advancing contact line is best generated by continual injection of liquid into the drop, e.g. by a hypodermic needle, while withdrawal of liquid causes a retreating contact line. Such methods are not practical for semiconductors and liquid metals, however, because of their easy oxidation when exposed to the atmosphere. Estimates of advancing and retreating contact angles can be obtained by tilting the surface on which the drop rests. When the drop just begins to roll down the surface, its profile yields estimates of both advancing and retreating contact angles.

REFERENCES³

1. L.L. Regel and W.R. Wilcox, "Detached Solidification in Microgravity: A Review," *Microgravity Sci. Technol.* **14**, 152-166 (1999).
2. W.R. Wilcox and L.L. Regel, "Detached Solidification," *Microgravity Science and Technology* **8**, 56-61(1995).
3. D.I. Popov, L.L. Regel and W.R. Wilcox, "Detached Solidification: 1. Steady-State Results at Zero Gravity," *J. Mat. Synth. & Proc.* **5**, 283-297 (1997).
4. D.I. Popov, L.L. Regel and W.R. Wilcox, "Detached Solidification: 2. Stability," *J. Mat. Synth. & Proc.* **5**, 299-311 (1997).
5. D.I. Popov, L.L. Regel and W.R. Wilcox, "Detached Solidification: 3. Influence of Acceleration and Heat Transfer," *J. Mat. Synth. & Proc.* **5**, 313-336 (1997).
6. Y. Wang, L.L. Regel and W.R. Wilcox, "Influence of Contact Angle, Growth Angle and Melt Surface Tension on Detached Solidification of InSb," *J. Crystal Growth* **209**, 175-180 (2000).
7. L.L. Regel, D.I. Popov and W.R. Wilcox, "Detached Solidification: Steady State Results," in *NASA Microgravity Materials Science Conference*, compiled by F. Szofran, D. McCauley and C. Walker, NASA CP-3342, Marshall Space Flight Center, pp 521-526 (1996).
8. L.L. Regel and W.R. Wilcox, "Detached Solidification," *Proceedings of the First Pan Pacific Basin Workshop on Microgravity Sciences*, *J. Jap. Soc. Microgravity Appl.* **15** (1998) 460-465.
9. L.L. Regel and W.R. Wilcox, "Improved Crystal Quality by Detached Solidification in Microgravity," in *Proceedings of the 1998 Microgravity Materials Science Conference*, compiled by D.C. Gillies and D.E. McCauley, NASA/CP-1999-209092, Marshall Space Flight Center, pp 533-540 (1999).
10. Y. Wang, L.L. Regel and W.R. Wilcox, "Steady State Detached Solidification of Water at Zero Gravity," *J. Crystal Growth* **226**, 430-435 (2001).
11. T. Duffar, P. Boiton, P. Dusserre and J. Abadie, "Crucible de-wetting during Bridgman growth in microgravity. II. Smooth crucibles," *J. Crystal Growth* **179**, 397-409 (1997).
12. I. Harter, P. Dusserre, T. Duffar, J.P. Nabot and N. Eustathopoulos, "Wetting of III-V metals on crucible materials," *J. Crystal Growth* **131**, 157-164 (1993).
13. J.V. Naidich, "The Wettability of Solids by Liquid Metals," in volume 14 of *Progress in Surface and Membrane Science*, edited by D. A. Cadenhead and J. F. Danielli, Academic Press, NY (1981) pp 354-484.
14. H. Taimatsu, T. Tani and H. Kaneko, "Effect of oxygen on the wettability of sapphire by liquid palladium," *J. Mat. Sci.* **31**, 6383-6387 (1996).
15. A. Sharan and A. W. Cramb, "Surface Tension and Wettability Studies of Liquid Fe-Ni-O Alloys," *Met. Mat. Trans. B* **28B**, 465-472 (1997).
16. D. Li and A. W. Neumann, "Contact Angles on Hydrophobic Surfaces and their Interpretations," *J. Colloid Interface Sci.* **148**, 190-200, (1992).
17. D. Li, M. Xie and A. W. Neumann, "Vapour Adsorption and Contact Angles on Hydrophobic Solid Surfaces," *Colloid Polymer Sci.* **271**, 573-580, (1993).
18. Y. Rotenberg, L. Boruvka and A. W. Neumann, "Determination of Surface Tension and Contact Angle from the Shapes of Axisymmetric Fluid Interfaces," *J. Colloid Interface Sci.* **93**, 169-183 (1983).

³ Each section has its own references.

19. R.E. Johnson, Jr. and R.H. Dettre, "Wettability and Contact Angles," in volume 2 of *Surface and Colloid Science*, edited by E. Matijevic, Wiley-Interscience, NY (1969) pp 85-153.
20. A.W. Neumann, "Contact Angles," in *Wetting, Spreading and Adhesion*, edited by J.F. Padday, Academic Press, NY (1978) pp 3-35.
21. R.J. Good, "Contact Angles and the Surface Free Energy of Solids," in volume 11 of *Surface and Colloid Science*, edited by R.J. Good and R.R. Stromberg, Plenum Press, NY (1979) pp 1-29.
22. R. Balasubramanian and W.R. Wilcox, "Surface Tension and Contact Angle of Molten Cadmium Telluride," *Int. J. Thermophys.* **11**, 25-35 (1990).
23. R. Shetty, R. Balasubramanian and W.R. Wilcox, "Surface Tension and Contact Angle of Molten Semiconductor Compounds: 1. Cadmium Telluride," *J. Crystal Growth* **100**, 51-57 (1990).
24. R. Shetty, R. Balasubramanian and W.R. Wilcox, "Surface Tension and Contact Angle of Molten Semiconductor Compounds: 2. Gallium Arsenide," *J. Crystal Growth* **100**, 58-62 (1990).
25. A. Katty, P. Dusserre, R. Triboulet and T. Duffar, "Surface tension of II-VI compounds and contact angle on glassy carbon," *J. Crystal Growth* **118**, 470-472 (1992).
26. B. LaPlane, "Mouillabilit  et Tension Superficielle de Mat riaux Semi-Conducteurs," Centre National de Recherche Scientifique, Meudon, France (1978).
27. R. Sangiorgi and M.L. Muolo, "Energetics and reactivity of liquid silicon-silica interface," *Mater. Sci. Forum (International Ceramics Conference)* (1998) pp 427-432.
28. B.R. Bathey, G.F. Hurley and H.E. Bates, "Observations of EFG Die Material Interactions with Liquid Silicon," *J. Mater. Sci.* **15**, 2192-6 (1980).
29. Y. Hayasaka, K. Edamura, M. Iwai, N. Onogawa and K. Kinoshita, "Evaluation of the Wettability of Molten InGaAs," *J. Jap. Soc. Microgravity Appl.* **14**, 101-102 (1997).
30. T.D. Blake and J.M. Haynes, "Contact Angle Hysteresis," in volume 6 of *Progress in Surface and Membrane Science*, edited by J. F. Danielli et al., Academic Press, NY (1973) pp 125-138.
31. J.F. Joanny and P.G. de Gennes, "A Model for Contact Angle Hysteresis," *J. Chem. Phys.* **81**, 552-562 (1984).
32. L.W. Schwartz and S. Garoff, "Contact Angle Hysteresis on Heterogeneous Surfaces," *Langmuir* **1**, 219-230 (1985).
33. M.O. Robbins and J.F. Joanny, "Contact Angle Hysteresis on Random Surfaces," *Europhys. Lett.* **3**, 729-735 (1987).
34. A. Marmur, "Contact Angle Hysteresis on Heterogeneous Smooth Surfaces," *J. Colloid Interface Sci.* **168**, 40-46 (1994).
35. A. Marmur, "Thermodynamic Aspects of Contact Angle Hysteresis," *Adv. Colloid Interface Sci.* **50**, 121-141(1994).
36. S. Brandon and A. Marmur, "Simulation of Contact Angle Hysteresis on Chemically Heterogeneous Surfaces," *J. Colloid Interface Sci.* **183**, 351-355 (1996).
37. C.W. Extrand and Y. Kumagai, "An Experimental Study of Contact Angle Hysteresis," *J. Colloid Interface Sci.* **191**, 378-383 (1997).
38. A. Seidl, R. Marten and B. M ller, "Development of an Electrochemical Oxygen Sensor for Czochralski Silicon Melts," *J. Electrochem. Soc.* **141**, 2564-2566 (1994).
39. Y. Matsushita and K. Goto, "On the Application of the Oxygen Concentration Cells with the Solid Electrolyte ZrO₂-CaO to the Basic Research Works in Process Metallurgy," *J. Fac.*

- Engin., U. Tokyo B 27, 217-280 (1964).
40. T.A. Hoffman, private communication, Illinois Instruments, Inc., Ingleside, IL (2001).
 41. Y. Wang, L.L. Regel and W.R. Wilcox, "Approximate Material Balance Solution to the Moving Meniscus Model of Detached Solidification," J. Crystal Growth 243, 546-560 (2002).
 42. Y. Wang, L.L. Regel and W.R. Wilcox, "Can propagation of gas bubbles lead to detached solidification? Experiments on freezing of water," Crystal Growth & Design 2, 453-461 (2002).
 43. J. Wang, L.L. Regel and W.R. Wilcox, "Detached solidification of InSb on Earth," J. Crystal Growth 260, 590-599 (2004).
 44. L.L. Regel, W.R. Wilcox, Y. Wang and J. Wang, "Improved Crystal Quality by Detached Solidification in Microgravity," Proceedings of the NASA 2002 Microgravity Materials Science Conference, NASA/CP -2003-212339, edited by D. Gillies, N. Ramachandran, K. Murphy, D. McCauley, and N. Bennett, pp 476-484 (2003).
 45. L.L. Regel, W.R. Wilcox, S. Ramakrishnan and A. Kota, "Residual Gas Effects on Detached Solidification in Microgravity," *ibid*, pp 688-694 (2003).

2. INTERACTION OF OXYGEN WITH MOLTEN Ga-DOPED InSb

Sessile drop experiments were performed on molten InSb containing ~0.1%Ga on clean quartz (fused silica) surfaces. A cell was constructed through which a mixture of argon, oxygen, and sometimes hydrogen were flowed. When the oxygen partial pressure exceeded approximately 10^{-6} bar in the absence of hydrogen, oxide formed on the surface of the melt that prevented it from deforming or moving on the substrate. This oxide was highly enriched in Ga. Reduction of the oxygen pressure or addition of 10% hydrogen to the argon caused the oxide to dissociate so that a shiny drop formed that easily moved across the substrate when the apparatus was tapped or the substrate was tilted slightly. Experiments performed on such shiny drops revealed that the surface tension of the molten InSb decreased with increasing hydrogen and oxygen partial pressures, and was relatively independent of temperature. It was estimated that this oxygen influence was caused by adsorption of $\frac{1}{4}$ of a monolayer of oxygen on the melt surface. The contact angle on quartz decreased with increasing oxygen pressure, and was relatively independent of hydrogen pressure or temperature, indicating that the solid-melt surface energy also was decreased by adsorbed oxygen. Both surface tension and contact angle appeared to vary with the square root of the oxygen partial pressure, indicating that oxygen dissociates when it dissolves in or adsorbs on the InSb. Raising the temperature caused a momentary decrease in oxygen concentration in the exit gas. This was attributed to adsorption of additional oxygen onto the surface of the melt. Tapping the apparatus increased the contact angle by about 0.6° , presumably because tapping overcame contact line sticking. Contact line sticking also caused a few degrees difference in upper and lower contact angles when the substrate was tilted until the drop rolled down.

2.1. Introduction

In Bridgman crystal growth of semiconductors, quartz ampoules are typically used that have been evacuated and backfilled with helium or argon. Even when a quartz ampoule is sealed with a high vacuum, outgassing and even diffusion through the ampoule wall lead to a residual gas pressure on the order of 10 Torr (~0.01 bar) [1-3,35]. Several percent of hydrogen is frequently added to avoid formation of oxide that can cause sticking of the crystal to the ampoule wall as well as formation of grains, twins and precipitates. Addition of H_2 to avoid oxide was essential in achieving detached solidification of Ga-doped InSb on Earth [5]. HgZnTe grew detached if a carbon getter was included in the ampoule [6,7].

Adsorbed impurities have been implicated in detached solidification through an increased contact angle θ , which theory indicates should favor detachment (e.g., [8,9]). Duffar *et al.* [10] claimed that *"semiconductors can present very high contact angles on crucible materials, due to slight amounts of pollution by residual gases. This phenomena is used to explain the de-wetting of semiconductors observed when grown under microgravity conditions in smooth crucibles."* The basis for this conclusion is their observation made in sessile drop experiments with InSb on silica [10]. As described in [9], *"it was practically always necessary to shake the molten drops a little bit in order to measure the contact angle corresponding to thermodynamic equilibrium (112° in this particular case), otherwise contact angles as high as 170° might have been measured. This effect is attributed to absorption of some impurity at the surface of the drop which creates a layer subsequently removed when shaking. In any case this layer cannot be*

confused with a solid peel on the drops which were always perfectly clean and shiny before, during and after the experiments. The vacuum in the ampoules during sealing was below 10^{-7} mbar." The most likely impurity that interacts strongly with molten semiconductors is oxygen.

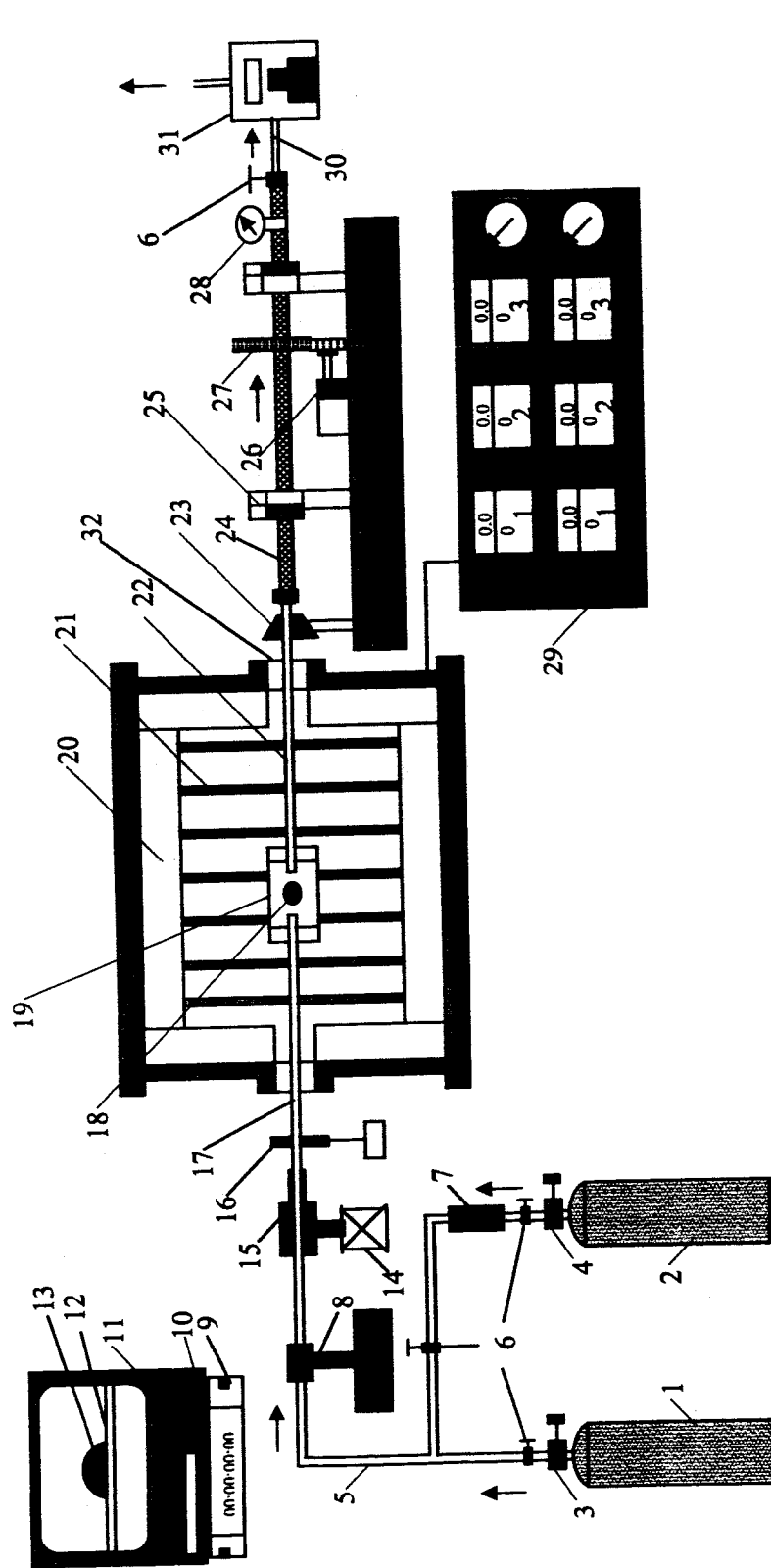
Numerous experiments with liquid metals on oxide surfaces have shown that dissolved oxygen always lowers the contact angle as well as the surface tension of the melt-gas interface [e.g., 11-14]. Silicon is the only semiconductor for which the influence of an impurity on surface properties has been extensively investigated. Sessile drop experiments showed that oxygen lowers the surface tension of molten silicon [15-19]. Huang *et al.* displayed their data versus the partial pressure of oxygen [15], while Niu *et al.* correlated their results versus the square root of the oxygen pressure based on oxygen dissociating upon entering molten Si [16-18]. Huang *et al.* also found that the contact angle of the melt on pyrolytic boron nitride decreased with increasing oxygen partial pressure, and measured higher oxygen and boron concentrations on the surface of frozen drops than in their interior [15]. Kaiser *et al.* attributed a slow decline in contact angle of germanium on oxide substrates to dissolution of oxygen in the melt [20].

2.2. Experimental apparatus and methods

Details of the experimental apparatus and methods are given elsewhere [21,22]. A schematic diagram of the apparatus is shown in Fig. 2.1. It consisted of the following parts:

- A Thermcraft three-zone split tube furnace to melt the InSb and maintain the resulting drop at the desired temperature.
- A cell containing a fused silica substrate to support the sessile drop (Fig. 2.2).
- A system to flow a gas of desired composition through the cell.
- An oxygen analyzer to measure the fugacity (partial pressure for an ideal gas) of oxygen in the gas flowing out of the cell.
- Supporting structures to hold the cell suspended in the furnace and a motor-gear assembly to tilt the cell.
- An optical system to videotape the drop profile during the experiment.

Several gas mixtures were used in the experiments, including regular industrial-grade argon, ultra-high purity (UHP) argon, UHP argon premixed with 10% hydrogen, argon with 3-ppm O_2 added, and argon with 6-ppm O_2 . Argon is extracted from air by distillation. Since the vapor pressures of oxygen and argon do not differ widely, it is virtually impossible to remove all oxygen from argon. Our gas supplier (Merriam-Graves Industrial Gases and Welding Products) specifies their industrial grade argon as containing <8-ppm O_2 and <5-ppm moisture, and their ultra-high purity argon with <1-ppm O_2 and <5-ppm moisture. An Oxisorb® oxygen-getter unit from Messer Griesheim (Krefeld, Germany) was used in some experiments to reduce the oxygen content of the argon. Oxisorb is claimed to remove both moisture and oxygen, to yield an oxygen concentration <0.1 ppm.



- | | | | |
|---|------------------------------|---|---------------------------------------|
| 1: Ar with desired O ₂ content | 10: VCR | 19: Chamber with fused silica substrate | 28: Pressure gauge |
| 2: Mixture of 90%Ar and 10%H ₂ | 11: Monitor | 20: Furnace insulation | 29: Temperature controller |
| 3: CGA 580 pressure regulator | 12: Substrate in the display | 21: SiC heating elements | 30: 1/8" stainless steel tube |
| 4: CGA 350 pressure regulator | 13: InSb drop in the display | 22: Outlet tube of cell | 31: Oxygen analyzer |
| 5: 1/2" copper tube | 14: Optical bench | 23: Light source | 32: Optical quality fused silica disc |
| 6: Ball valve | 15: Camera with the lens | 24: 1/2" stainless steel pipe | |
| 7: Oxisorb | 16: Filter | 25: Bearings | |
| 8: Inlet support | 17: Inlet tube of cell | 26: Motor | |
| 9: Time code generator | 18: InSb sessile drop | 27: Gear | |

Figure 2.1. Sessile drop apparatus

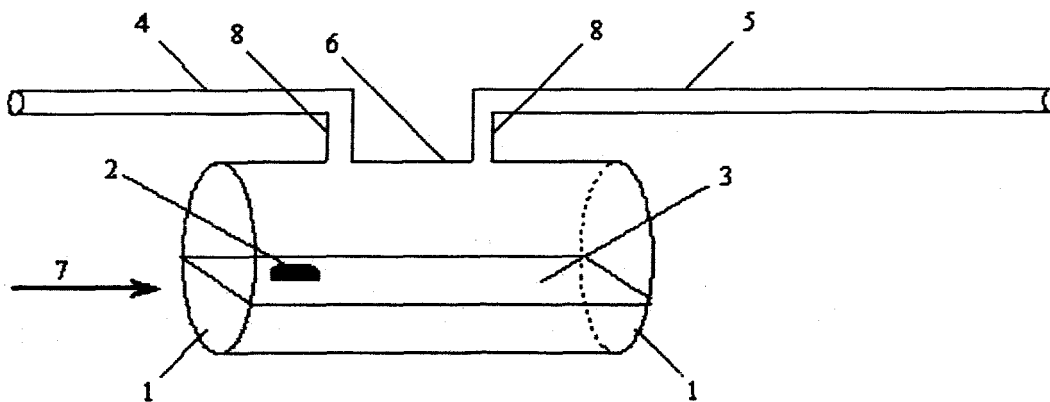


Figure 2.2. Schematic diagram of the cell.

1. Ground and polished optical quality fused silica discs (30 mm ID x 32 mm OD).
2. InSb sessile drop.
3. Fused silica microscope slide (75 mm x 25 mm).
4. Fused silica inlet gas tube (8 mm ID, 10 mm OD and 70 cm long).
5. Fused silica outlet gas tube (8 mm ID, 10 mm OD and 70 cm long).
6. Fused silica cylinder (30 mm ID, 32 mm OD and 75 mm long).
7. View of the CCD video camera.
8. Riser for inlet and outlet gas tubes (15 mm long).

The oxygen fugacity in the gas flowing out of the experimental cell was measured by a DF-150 non-depleting coulometric oxygen analyzer from Delta-F Co. Such oxygen sensors are claimed to be the most efficient instruments to measure the oxygen content in gases, especially for trace amounts. They are more stable than galvanic sensors and the electrodes are non-depleting, as neither electrode undergoes chemical changes while oxygen is being measured. The DF-150 is able to measure oxygen concentrations between 0.01 ppm and 10 ppm, and requires a sample pressure between -5 and +5 psig, a sample flow rate between 1 and 5 standard cubic feet per hour (scfh), and an operating temperature between 5°C and 50°C. After purging the apparatus for 1 day with industrial argon the oxygen analyzer showed 0.6 to 0.7-ppm O₂, and gave 0.3-ppm O₂ purging with ultra-high purity argon.

Contact-line sticking can inhibit motion of a sessile drop, which probably accounts for the observation of Duffar *et al.* [9,10] quoted above. It also causes the contact angle of a moving drop to deviate from the equilibrium static value, increasing the contact angle at the advancing contact line and decreasing the contact angle at the retreating contact line. The difference between advancing and retreating contact angles is known as contact-angle hysteresis. An indication of contact-angle hysteresis can be obtained by tilting the substrate on which the drop rests. Contact-line sticking causes the upper contact angle to decrease and the lower contact angle to increase. As the substrate is tilted farther, eventually the contact-line sticking is insufficient to prevent the drop from rolling down the surface. The difference between upper and lower contact angles just prior to the commencement of drop movement is a measure of contact-angle hysteresis. Here, tilting of the cell containing the substrate was achieved by employing a motor-gear assembly attached to the gas tubing exiting the cell. When desired, the gear was

rotated with a 0.23 rpm synchronous motor, either clockwise or counterclockwise.

Our preliminary experiments revealed that excess vibration in our laboratory caused the surface of the sessile drop to shake, making measurement inaccurate. Additionally, in attempting to measure contact-angle hysteresis by tilting the substrate, the vibration led to premature rolling of the drop down the incline. Consequently, the end supports for the cell were placed on vibration damping pads with metal weights to depress the pads. This eliminated the vibration problem.

A Sony SSC-M374 black and white CCD camera fitted with a MLH 10X zoom lens was used to view the drop through the gas-entry end of the furnace. A light source (Sylvania 100 watt bare bulb) was placed at the other end of the furnace, so that the drop was seen as a silhouette. The CCD camera was connected to a P2 Time Traveler time code generator to insert the time on each frame. The view of the drop was displayed on a Videotek monitor and recorded using a Sanyo-4 Head/Field Advance videocassette recorder. A welding filter was placed between the CCD camera and the furnace to eliminate excessive light that otherwise caused haziness in the video picture. The camera assembly was mounted on an optical bench and could be moved in both directions perpendicular to the axis of view.

In the preliminary experiments, a reflection of the drop was observed on the surface of the substrate due to the misalignment between the axis of the camera lens and the surface of the substrate. This misalignment and the resulting reflection were eliminated by adjustment of the heights of the supports for the ampoule (See Fig. 2.3).

For an experiment, a weighed and cleaned sample of InSb was placed in the cell, which then was integrated into the gas-flow system. The gas flow was begun at about 1.6 scfh and a pressure of about 2 psig. The oxygen analyzer was turned on about 10 min after this gas purging was begun. Immediately after turning it on, the oxygen analyzer read about 11-ppm O₂. During the first few minutes the oxygen reading decreased rapidly, and subsequently decreased slowly. The furnace temperature was gradually raised to 550°C over a 6-h period. Videotaping of the drop was begun when the temperature reached 550°C and was continued throughout the experiment. After several hours, a shiny drop resulted, provided either the argon contained 10% hydrogen or had less than about 1 ppm of oxygen. Higher oxygen concentrations resulted in oxidized drops that adhered to the substrate and did not move when the apparatus was tapped or the substrate tilted, whereas shiny drops readily moved.

A gas purge time of 24 to 36 h was used in order to make certain the surface of the drop was clean and that the oxygen analyzer was reading a constant value. After this time, the gas exiting the cell should have had the same composition as that entering, and the sessile drop should have been in equilibrium with this gas. In all the experiments, as the gas in the cylinder was consumed, the outlet pressure from the pressure regulator gradually increased, causing the flow rate to slowly increase. At the same time, the oxygen concentration slowly decreased. The increase in pressure and decrease in oxygen concentration tended to compensate one another, so that the change in oxygen partial pressure (product of these two) was not large during an experiment.



Figure 2.3. Image of the drop from experiment 10 grabbed from the videotape.
Note that there is no reflection of the drop on the substrate surface.

After the sample had melted, the furnace temperature was changed stepwise over 30 h in the following cycle – 550°C, 600°C, 650°C, 600°C, 550°C. At each temperature, the entire experimental setup was left undisturbed for 6 to 8 h. Then the substrate was tilted counterclockwise until the drop rolled down. Figure 2.4 shows a drop in the video frame just prior to that in which the drop rolled down. The substrate was then rotated clockwise to bring the drop back into view and set to horizontal. This tilting process was repeated twice more. To measure the static contact angle, the inlet tube was tapped vigorously enough to cause the drop to jump slightly off the substrate. This was done in order to eliminate any contact-angle pinning, i.e., sticking of the contact line. After a few minutes, the temperature was changed to the next value in the cycle. When the cycle was completed, the power to the furnace was turned off while the gas flow continued until the furnace was at room temperature.

The analog signal from the videotape was transmitted to HLIImage++98 (Western Vision Software) image processing software, where it was converted to digital format and stored. The pixel data were retrieved, one frame at a time, using a DT3152 frame grabber from Data Translation Inc. For the determination of the static contact angle, three frames were selected from the videotape corresponding to each temperature before and after tapping the apparatus, i.e. 6 at each temperature. A program was written [21] in Matlab 6.1 to detect the edge of the drop using the Prewitt edge operator [25] in the Matlab image-processing toolbox. The resulting binary image was further processed using a C program to obtain the profile of the drop, i.e., the x and z coordinates of the drop edge [21]. The resulting coordinates were used in ADSA-P [26], which yields the surface tension and the contact angle best fitting the drop edge coordinates to the theoretical shape of this sessile drop in the gravitational field [27]. Contact-angle hysteresis was estimated using the digitization and image processing procedures above, followed by

aligning tangents on the two sides of the drop using HImage++98. The difference between the resulting two contact angles is defined here as contact-angle hysteresis.

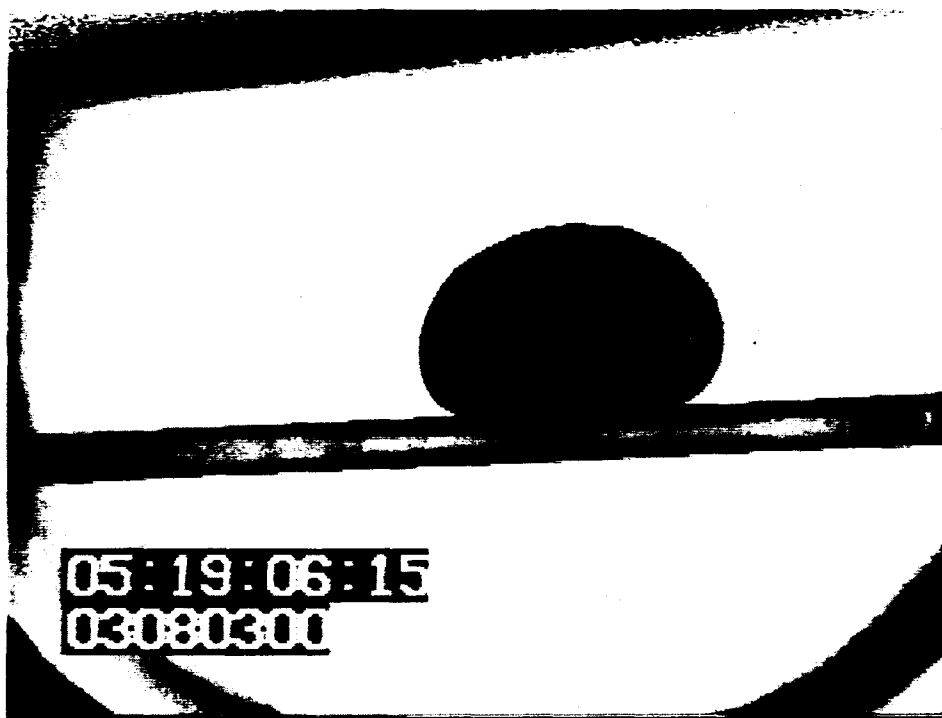


Figure 2.4. Image of the drop on a tilted substrate from experiment 12. This image was grabbed just before the drop rolled down the substrate.

2.3. Experimental results

Addition of hydrogen to the argon gas did not result in a decrease in oxygen concentration of the gas entering the oxygen analyzer.

When the furnace temperature was increased to the next higher value in the cycle, there was an almost instantaneous decrease of 0.02 to 0.05 ppm in the oxygen analyzer reading, which subsequently increased and stabilized at the value existing before the change in temperature. This all transpired in 1 to 2 min. When the temperature was decreased to the next lower value in the cycle, the reverse process occurred.

The frozen drops from the experiments were examined by optical microscopy, scanning electron microscopy (SEM) and energy dispersive x-ray spectroscopy (EDX) in the SEM. Each frozen drop was rounded with one or more protrusions, as shown in Fig. 2.5. Such protrusions are well known when group IV, III-V and II-VI semiconductors are frozen, and arise because the melt has a greater density than the corresponding solid. Some drops had rough black oxide coatings. Figure 2.6 shows a cross section of such a coating. As shown in Fig. 2.7, EDX spectra of these coatings displayed peaks not only for In, Sb and O, but also a strong peak for Ga. EDX of the starting material showed no Ga peak. Glow discharge mass spectroscopy of a piece of the starting material was performed by the Institute for National Measurement Standard, National Research Council, Canada, and showed approximately 0.1 atom% Ga. This Ga concentration is

below the detection limit for our EDX. As shown in Fig. 2.8, the ratio of Ga to In peak heights of the surface of frozen drops increased with increasing oxygen concentration during the experiment. That is, the enrichment of the oxide in Ga increased with increasing oxygen concentration in the gas. The data shown in Fig. 2.8 were correlated by three different equations:

$$\text{Ga / In} = 0.26 + 1.4 \times 10^5 P_{\text{O}_2} \quad R^2 = 0.84, p = 0.083 \quad (1)$$

$$\text{Ga / In} = 0.040 + 400 \sqrt{P_{\text{O}_2}} \quad R^2 = 0.87, p = 0.067 \quad (2)$$

$$\text{Ga / In} = 420 \sqrt{P_{\text{O}_2}} \quad R^2 = 0.87, p = 0.0020 \quad (3)$$

where Ga/In is the ratio of EDX peak heights, P_{O_2} is the oxygen partial pressure in bar, R^2 is the correlation coefficient squared, which is the fraction of the variation in Ga/In explained by the correlation, and p is the probability that the true slope was negative rather than positive as found. Thus, the best correlation is that giving the highest R^2 and the lowest p . For this reason, we chose to plot Ga/In versus the square root of the oxygen partial pressure in Fig. 2.8. Additionally, as shown later, the contact angle and surface tension also correlated best against $\sqrt{P_{\text{O}_2}}$.

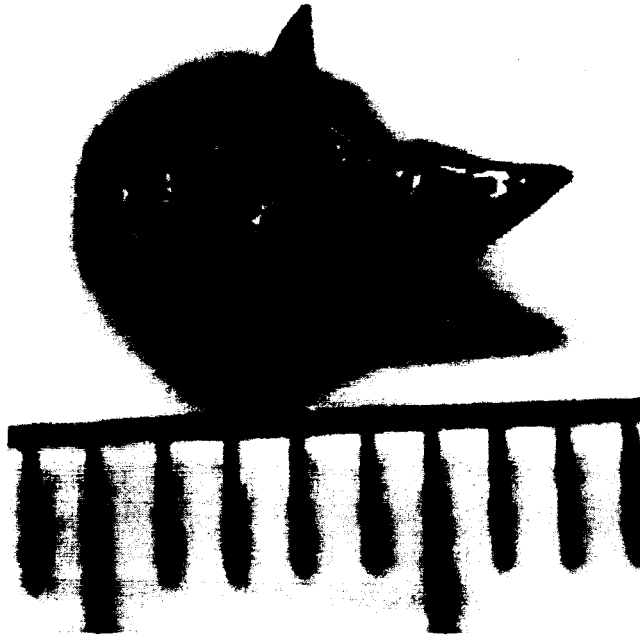


Figure 2.5. Image of a frozen InSb drop resulting from experiment 11. Notice that the edges of the sample are rounded and there are two shiny protrusions. The scale is in mm.

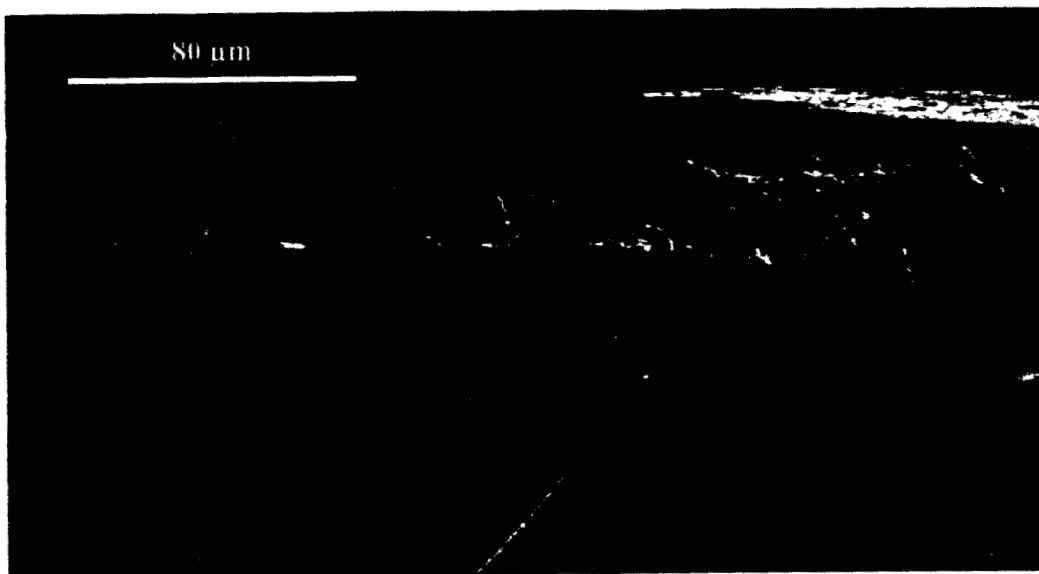


Figure 2.6. Cross section of a heavily oxidized frozen drop.
The oxide layer is about 40 μm thick.

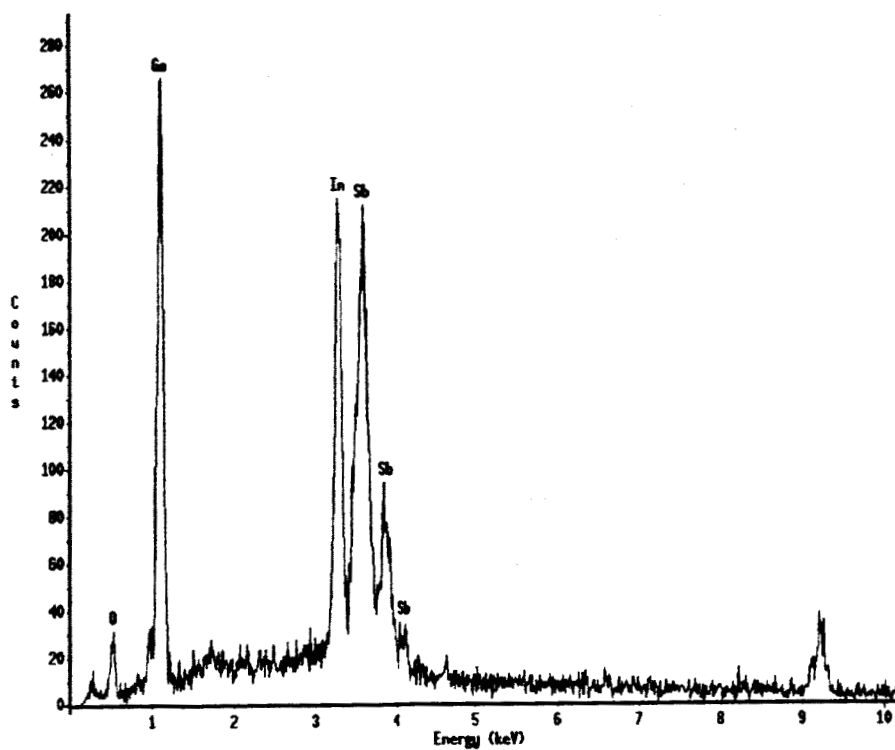


Figure 2.7. EDX spectra of the surface of an oxidized frozen drop.
Note the peaks for oxygen, gallium, indium and antimony.

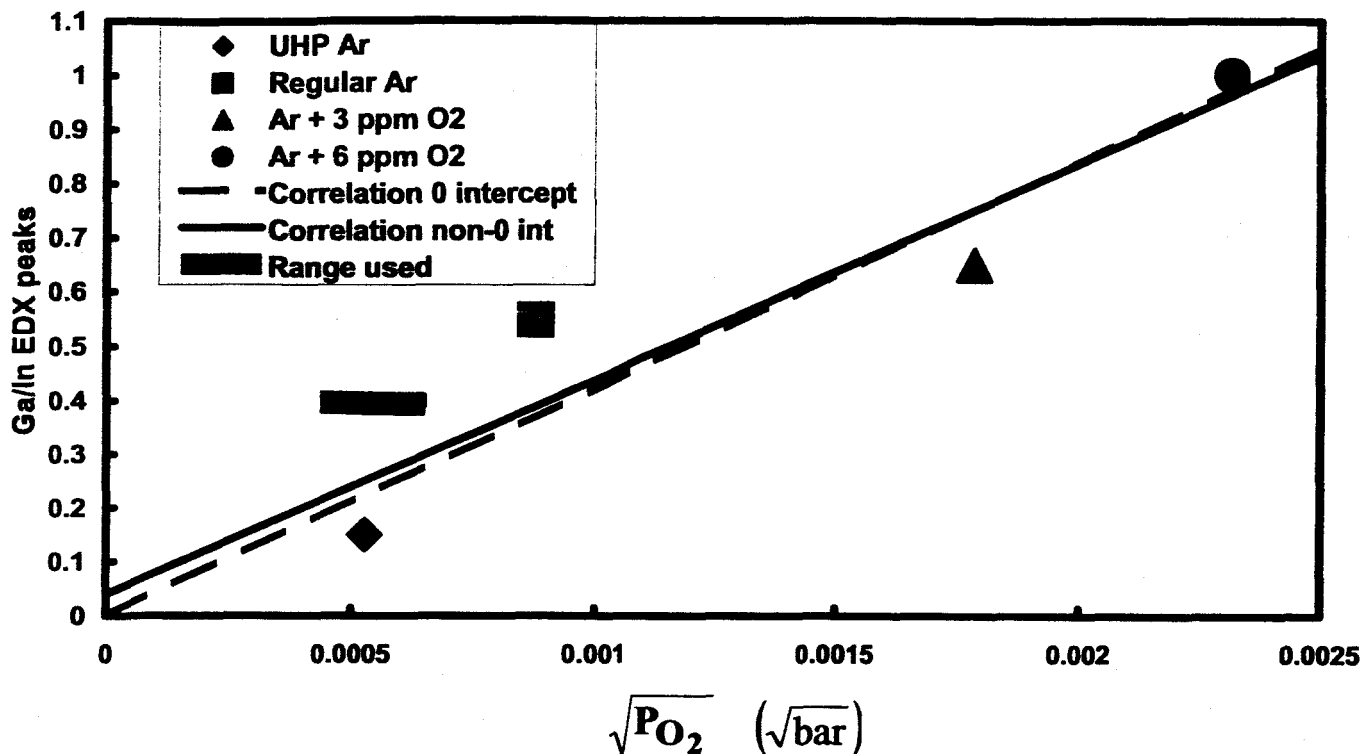


Figure 2.8. The influence of average oxygen fugacity (square root of oxygen partial pressure) during sessile-drop experiments on the ratio of the peak heights of Ga and In in the EDX spectra of dull portions of frozen drops. The gray bar shows the range of oxygen partial pressures used in the experiments from which contact angles and surface tensions were obtained.

Sessile drops that were shiny and moved easily on the substrate always had a dull surface when they were frozen. Scanning electron microscopy of frozen drops revealed dark islands, as shown in Fig. 2.9. The size of these islands was smaller when 10% hydrogen had been added to the gas. EDX spectra of these dull regions showed Ga and O peaks. Thus, the black islands are believed to be oxide. Whether these were present during the experiment or formed during cooling and freezing is uncertain. The protrusions that were ejected during freezing remained shiny and showed no Ga or O EDX peaks.

There were five experiments (out of many) in which everything worked perfectly to obtain good sessile drop data: the drops remained shiny during the experiment, moved easily, and gave good images for analysis. Multiple regression analysis showed that the temperature dependence of contact angle and surface tension was less than the scatter in the data. The surface tension was independent of tapping on the inlet tube, while the contact angle increased by an average of 0.6° after tapping. Since tapping tends to eliminate the influence of contact-line sticking and gives values nearer equilibrium, only data after tapping were used to correlate the contact-angle data. Both surface tension and contact angle decreased with increasing oxygen concentrations, as shown in Figs. 2.10 and 2.11.

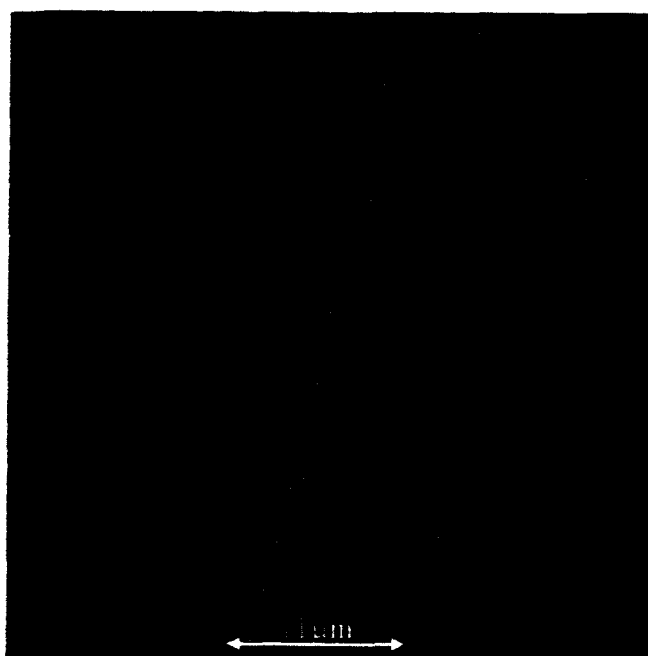


Figure 2.9. Scanning electron micrograph of a dull portion of the frozen drop from experiment 14. The black islands are believed to be oxide.

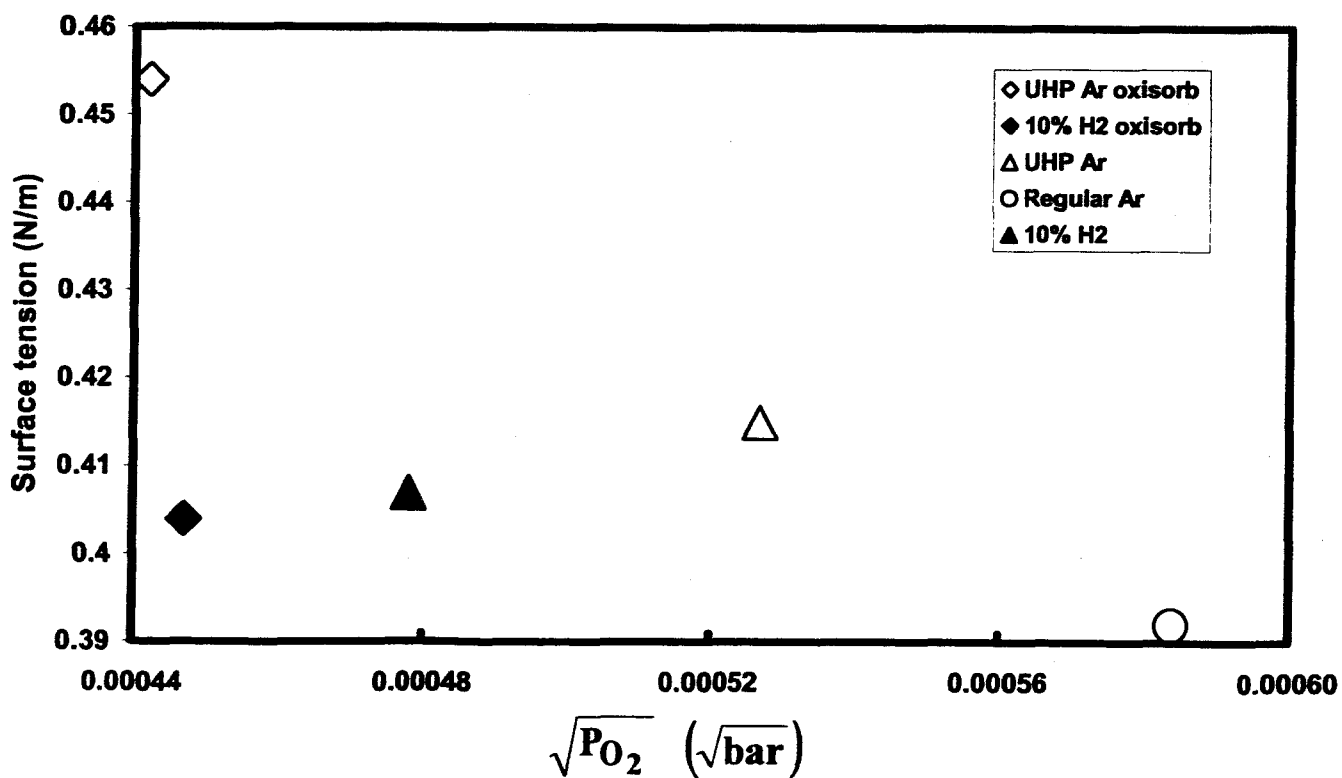


Figure 2.10. Average surface tension versus the average square root of the oxygen partial pressure in the five successful sessile drop experiments.

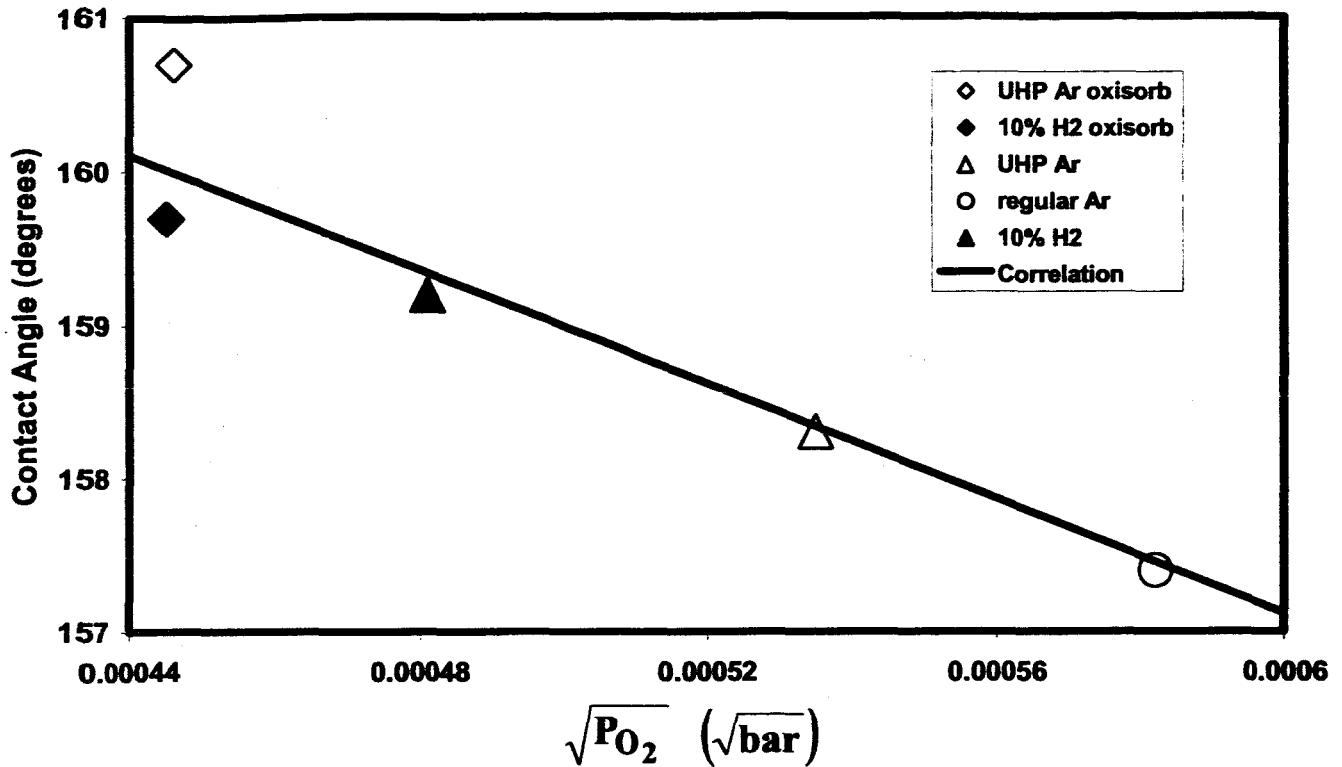


Figure 2.11. Average contact angle versus the average square root of the oxygen partial pressure in the five successful sessile drop experiments.

The surface tension was decreased by adding H_2 , while contact angle was unaffected by H_2 . Correlations obtained versus the square root of oxygen partial pressure were far superior (much higher R^2) to linear relationships. Since hydrogen was either absent or at 0.1 mole fraction, we were unable to distinguish between linear and square root dependences on H_2 partial pressure. The final correlating relationship for surface tension from 123 data points was:

$$\gamma_{vl} = 0.60 - 0.015P_{H_2} - 350\sqrt{P_{O_2}} \quad R^2 = 0.58, p_H = 4 \times 10^{-16}, p_O = 6 \times 10^{-24} \quad (4)$$

where γ_{vl} is the melt surface tension in N/m, P_{H_2} is the hydrogen partial pressure in bar, p_H is the probability that the coefficient for P_{H_2} is positive, and p_O is the probability that the coefficient for $\sqrt{P_{O_2}}$ is positive. The 95% confidence limits for the coefficient for P_{H_2} are -0.019 and -0.012, i.e. there's a 95% probability that the true slope lies between these values. The 95% confidence limits for the coefficient for $\sqrt{P_{O_2}}$ are -410 and -300. The final correlating relationship for contact angle from 66 data points was:

$$\theta = 170 - 1.9 \times 10^4 \sqrt{P_{O_2}} \quad R^2 = 0.29, p = 3 \times 10^{-6} \quad (5)$$

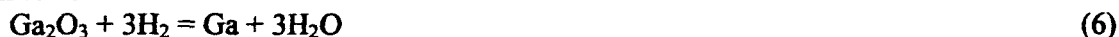
where θ is the contact angle in degrees. The 95% confidence limits for the coefficient for $\sqrt{P_{O_2}}$ are -2.6×10^4 and -1.1×10^4 .

The angle of tilt at which the drop rolled down the silica substrate ranged from 0.005 to 8.2°, and averaged 1.5°. The lower contact angle just prior to rolling down ranged from 155 to 162°, with

an average of 158°. The upper contact angle just prior to rolling down ranged from 146 to 156°, with an average of 151°. The hysteresis ranged from 1 to 14°, and averaged 7°. There was negligible correlation of these parameters with one another and with temperature, oxygen partial pressure, hydrogen partial pressure.

2.4. Discussion and Conclusions

Addition of hydrogen did not measurably reduce the oxygen concentration in the exiting gas, indicating that negligible reaction between hydrogen and oxygen occurred.⁴ The residence time for the gas in the cell was approximately 2.4 s. On the other hand, addition of 10% hydrogen reduced problems with oxide formation on the drops. It is common to add hydrogen to the backfill gas in crystal growth, and experience shows that this greatly diminishes problems with oxide. Our results indicate that hydrogen directly reduced the oxide on our material, through a reaction such as



even though the hydrogen did not lower the oxygen concentration in the gas.

Gallium was concentrated in the oxide, which is not surprising because of the greater (negative) free energy of formation of Ga_2O_3 than for In_2O_3 and Sb_2O_4 [29]. This phenomenon became more pronounced as the oxygen concentration in the gas was increased. One would also expect, therefore, that oxidation problems would become more severe as the Ga content of InSb is increased.

At an oxygen partial pressure on the order of 10^{-7} bar, the average value of the vapor-liquid surface tension γ_{vl} was about 0.41 N/m. Harter *et al.* [10] reported the surface tension near the melting point to be 0.43 N/m for InSb sealed in an ampoule with an oxygen partial pressure less than 5×10^{-10} bar, but with a pressure of approximately 10^{-5} bar upon opening the ampoule. Lazrev *et al.* [30,31] reported the surface tension near the melting point to be 0.42 N/m. Thus our surface tension results are consistent with those in the literature for InSb, indicating that its surface tension is not appreciably influenced by 0.1% Ga in the melt.

We found that the surface tension decreased with the square root of the oxygen partial pressure. When an impurity causes a surface energy to decrease, it is because the system free energy is lowered by adsorption of the impurity on the surface. The relationship between surface excess Γ and surface energy γ is known as the Gibbs Adsorption equation (e.g., [32]):

$$\Gamma = - \left(\frac{\partial \gamma}{\partial \ln f} \right)_T / RT \quad (7)$$

where R is the gas constant, T absolute temperature, and f the fugacity (partial pressure for an ideal gas) of the adsorbing species. Recorrelating the surface tension versus the log of the oxygen fugacity (partial pressure), we find $(\partial \gamma_{vl} / \partial \ln f) \approx -0.092$ N/m and from Eq. 7, $\Gamma = 1.27 \times 10^{-5}$ mol O_2/m^2 . The Gibbs Adsorption equation provides no information on the state of the adsorbed gas nor on how many atomic layers this excess amount of oxygen is spread. However, the observed dependence of surface tension on the square root of the oxygen partial pressure indicates that the oxygen dissociates into atomic or ionic form. This would be expected if

⁴ At equilibrium this reaction would be essentially complete. For example, with 10% H_2 and 100 ppm O_2 supplied with Ar at 1 atm and 600°C the calculated equilibrium mole fraction of O_2 is approximately 10^{-29} .

molten InSb behaves as a metal, because diatomic gases are known to dissociate upon dissolving in molten metals, giving rise to a solubility that depends on the square root of the partial pressure of the gas (Sieverts' Law [28,33]). We estimate the monolayer concentration by using the O^{2-} crystal ionic radius, which is 1.32 Å [34]. Thus, for a square array of oxygen ions, the monolayer concentration is approximately:

$$\left[\frac{O^{\equiv} \text{ion}}{(1.32 \times 10^{-10} \text{ m})^2} \right] \left(\frac{O_2 \text{ molecule}}{2 O^{\equiv} \text{ions}} \right) \left(\frac{\text{mol } O_2}{6.023 \times 10^{23} O_2 \text{ molecules}} \right) = 4.8 \times 10^{-5} \left(\frac{\text{mol } O_2}{\text{m}^2} \right) \quad (8)$$

Thus, Γ represents about 1/4 of a monolayer. This seems reasonable.

Changing the temperature caused momentary changes in the oxygen concentration in the outlet gas. When the temperature was increased, the oxygen concentration decreased, and *vice versa*. One possible explanation is that the melt absorbed (dissolved) oxygen when the temperature was increased and *vice versa*, due to the solubility of oxygen in InSb increasing with temperature. This would be reasonable as the solubility of oxygen in liquid metals usually increases with increasing temperature, i.e., dissolution in liquid metals is usually endothermic (e.g., [28]). However, the observation was that the oxygen concentration change was almost instantaneous. If exchange with the interior of the molten drop is required, then diffusion through the drop must occur and that would be relatively slow. Another possibility is that exchange occurred with oxygen adsorbed on the drop surface, with the surface excess increasing with increasing temperature. While such exchange requires no diffusion and so should be rapid, we need to confirm that there was sufficient surface excess for this to be reasonable. We compare estimates of the change in moles of oxygen resulting from a temperature change with the total moles of oxygen adsorbed on the drop. Let us assume a flow rate of 1.6 scfh, a change in oxygen concentration of 0.035 ppm for 1 s, and a temperature of 873 K. The ideal gas law then gives the amount of oxygen released into the gas as:

$$\left(\frac{1.6 \text{ ft}^3 \text{ Gas}}{\text{h}} \right) \left(\frac{\text{h}}{3600 \text{ s}} \right) (1 \text{ s}) \left(\frac{0.035 \times 10^{-6} \text{ mol } O_2}{\text{mol Gas}} \right) \left(\frac{\text{mol Gas} \cdot \text{K}}{0.00290 \text{ atm} \cdot \text{ft}^3 \text{ Gas}} \right) \left(\frac{1 \text{ atm}}{873 \text{ K}} \right) = 7.4 \times 10^{-12} \text{ mol } O_2 \quad (9)$$

The total amount of oxygen adsorbed on the drop is estimated by assuming the drop is hemispherical with a mass of 0.4 g and a density of 6.5 g/cm³:

$$\left(\frac{1.27 \times 10^{-5} \text{ mol } O_2}{\text{m}^2} \right) 2\pi \left(\frac{3 \times 0.4 \text{ g}}{2\pi \times (6.5 \text{ g/cm}^3)} \right)^{2/3} \left(\frac{\text{m}}{100 \text{ cm}} \right)^2 = 7.6 \times 10^{-10} \text{ mol } O_2 \quad (10)$$

Thus, the change in oxygen in the gas exiting the cell after a temperature change was only about 1% of the oxygen adsorbed on the drop. This does not preclude some exchange with oxygen dissolved in the bulk melt.

The static contact angle found here was about 159° while the upper and lower contact angles

from the tilting experiments were slightly lower. This is compared to 112° determined by Harter *et al.* [10] using a sessile drop technique. This is a large discrepancy and the reason for it is unknown, although it should be noted that our static and tilting contact angles were almost the same even though they were obtained using two quite different image processing methods. Perhaps the small amount of gallium in our sample could account for our larger value because of vastly altered interactions with the silica substrate. Consequently, we are performing additional experiments with more pure InSb.

Here, the contact angle also was observed to decrease with the square root of the oxygen partial pressure, indicating that dissociated oxygen was responsible for the decrease. The classical relationship Young equation between surface energies and contact angle θ is:

$$\cos \theta = \frac{\gamma_{sv} - \gamma_{sl}}{\gamma_{lv}} \quad (11)$$

where γ_{sv} is the energy (J/m^2) of the solid-vapor surface, γ_{sl} is the energy of the solid-melt surface, and γ_{lv} is the energy (surface tension) of the melt-vapor surface. For $\theta > 90^\circ$ as observed here, $\cos \theta < 0$, indicating that $\gamma_{sl} > \gamma_{sv}$. We have shown that oxygen decreases γ_{lv} . If γ_{sv} and γ_{sl} were unchanged by oxygen, the decrease in γ_{lv} would cause θ to increase. Since θ decreased, either γ_{sv} was increased or γ_{sl} was decreased by oxygen. It is thought unlikely that γ_{sv} is appreciably influenced by oxygen, and much more reasonable that oxygen acts to lower γ_{sl} , perhaps by adsorption of oxygen ions on the silica surface. Similar behavior has been observed for the surface tension and contact angle of liquid metals in the presence of oxygen (e.g., [12]).

Even for drops that remained shiny and mobile during an experiment, islands of oxide (Fig. 2.9) formed dull sections when these were frozen, while the extruded protrusions remained oxide free. One possibility is that these oxide patches formed as the drops were cooled because of reduced oxygen adsorption and reduced solubility in the melt. Another possibility is that the oxide islands were present on the molten drop during experiments. The apparent lack of agglomeration of these islands suggests that they repelled one another, probably because of adsorption of O^- ions. One could argue that this would decrease the effective surface tension of the melt, with increasing oxygen in the gas causing more oxide islands and decreasing the measured surface tension. However, hydrogen was observed to decrease these oxide islands and so by this argument would have increased the surface tension. Rather, hydrogen decreased surface tension, perhaps by adsorbing on the surface of the melt.

Addition of hydrogen did not noticeably influence the contact angle θ . Perhaps the increase in θ caused by the decrease in γ_{lv} was compensated for by a decrease in θ through an increase in γ_{sl} . One might imagine that H^+ dissolved in the melt causes less adsorption of O^- on the silica surface.

The variation in contact-angle hysteresis can be explained by the influence of microheterogeneities on the silica substrate. Contact-angle hysteresis is usually attributed to such heterogeneities, which vary over a substrate surface. The drop was in a different location in each experiment and would have experienced different heterogeneities.

References

1. W. Palosz, *J. Crystal Growth* 191 (1998) 897-903.
2. W. Palosz, *Proceedings of SPIE 3123 - Materials Research in Low Gravity* (1997) 34-43.
3. W. Palosz, *J. Jpn. Soc. Microgravity Appl.* 15 (1998) 454-459.
4. L.L. Regel, W.R. Wilcox, *Microgravity Sci. Technol.* 14 (1999) 152-166.
5. J. Wang, L.L. Regel, W.R. Wilcox, *J. Crystal Growth* (submitted).
6. M.P. Volz, M. Schweizer, N. Kaiser, S.D. Cobb, L. Vujisic, S. Motakef, F.R. Szofran, *J. Crystal Growth* 237-239 (2002) 1844-1848.
7. S.D. Cobb, F.R. Szofran, K.S. Jones, S.L. Lehoczy, *J. Electron, Mat.* 28 (1999) 732-739.
8. Y. Wang, L.L. Regel, W.R. Wilcox, *J. Crystal Growth* 143 (2002) 546-560.
9. T. Duffar, P. Boiton, P. Dusserre and J. Abadie, "Crucible de-wetting during Bridgman growth in microgravity. II. Smooth crucibles," *J. Crystal Growth* 179, 397-409 (1997).
10. I. Harter, P. Dusserre, T. Duffar, J.Ph. Nabot and N. Eustathopoulos, *J. Crystal Growth* 131, 157-164 (1993).
11. N. Eustathopoulos, M.G. Nicholas, B. Drevet, *Wettability at High Temperatures*, Pergamon/Elsevier, Oxford (1999) pp 218-239.
12. Ju.V. Naidich, *Progress in Surface and Membrane Science*, edited by D.A. Cadenhead and J.F. Danielli, Academic Press, NY, Volume 14 (1981) pp 354-484.
13. H. Taimastu, T. Tani and H. Kaneko, *J. Mat. Sci.* 31 (1996) 6383-6387.
14. A. Sharan and A.W. Cramb, *Met. Mat. Trans. B* 28B (1997) 465-472.
15. X. Huang, S. Togawa, S. Chung, K. Terashima, S. Kimura, *J. Crytal Growth* 156 (1995) 52-58.
16. Z. Niu, K. Mukai, Y. Thiaishi, T. Hibiya, K. Kakimoto, M. Koyama, *J. Jpn. Assoc. Crystal Growth* 24 (1997) 31-40.
17. Z. Niu, K. Mukai, Y. Shiraishi, T. Hibiya, K. Kakimoto, M. Koyama, *Proceedings of the International Conference on High Temperature Capillarity*, edited by N. Eustathopoulos and N. Soczak, Cracow, Poland (1997) 175-181.
18. Z. Niu, K. Mukai, Y. Shiraishi, T. Hibiya, K. Kakimoto, M. Koyama, *Proceedings of the Joint Xth European and VIth Russian Symposium on Physical Sciences in Microgravity*, edited by V.S. Avduyevsky and V.I. Polezhaev, Moscow II (1997) 48-55.
19. M. Ratto, E. Ricci, E. Arato, *J. Crystal Growth* 217 (2000) 233-249.
20. N. Kaiser, A. Cröll, F.R. Szofran, S.D. Cobb, K.W. Benz, *J. Crystal Growth* 231 (2001) 448-457.
21. A.K. Kota, M.S. Thesis, Clarkson University, Potsdam, NY (2003).
22. S. Ramakrishnan, M.S. Thesis, Clarkson University, Potsdam, NY (2003).
23. A.W. Neumann, R.J. Good, in *Surface and Colloid Science*, edited by R.J. Good and R.R. Stromberg, Plenum Press, NY, Vol. 11 (1979) p.31.
24. A. Carré, N. Visovsky, *J. Adhesion* 68 (1998) 301-313.
25. A.C. Bovik, *Handbook of Image and Video Processing*, Academic Press, San Diego, CA (2000).
26. S. Lahooti, O.I. Del Rio, A.W. Neumann, P. Cheng, in *Applied Surface Thermodynamics*, edited by A.W. Neumann, Marcel Dekker Inc., NY (1996).
27. F. Bashforth, J.C. Adams, *An Attempt to Test the Theory of Capillary Action*, Cambridge University Press, Cambridge, England (1892).
28. O. Kubaschewski, A. Cibula, D.C. Moore, *Gases and Metals*, American Elsevier Publishing Co., NY (1970) pp 11-18.
29. L.B. Pankratz, *Thermodynamic Properties of Elements and Oxides*, U.S. Government

- Printing Office, Washington, DC (1982).
30. V.B. Lazrev, Russian J. Phys. Chem., 38 (1964) p.172; through [10].
 31. M.Y. Dashevski, G.V. Kukuladze, V.B. Lazrev, M.S. Mirgalovskii, Izv. Akad. Nauk SSSR, Neorg. Mater., 3 (1967) p.1561; through [10].
 32. G.N. Lewis, R. Randall, K.S. Pitzer, L. Brewer, Thermodynamics, second edition, McGraw-Hill, NY (1961) p 485.
 33. A. Sieverts, Z. Metallkunde 21 (1929) 37-46.
 34. R.C. Weast, M.J. Astle, W.H. Beyer, CRC Handbook of Chemistry and Physics, 66th edition, CRC Press, Boca Raton, Florida (1985) p F-164.
 35. W. Palosz, Private Communications, BAE Systems, NASA Marshall Space Flight Center, AL 35812 (2003).

3. REVISED EXPERIMENTAL METHODS

The experiments reported in the previous section utilized Ga-doped InSb, could not reach sufficiently low oxygen concentrations. The methods for extracting contact angles from drop images produced excessive scatter in the data as well as values that exceeded those in the literature. The work described in this section was aimed at producing reliable results on high-purity InSb with much lower oxygen concentrations.

3.1. Experimental apparatus

The apparatus consisted of the following components:

1. A three-zone clamshell furnace with silicon carbide heating rods (Thermcraft Inc.). Each zone had its own temperature controller.
2. Supporting structures for the furnace over thick rubber pads to minimize vibration of the experiment cell.
3. A quartz (fused silica⁵) cell with a quartz microscopic slide for the InSb sample.
4. A motor-gear assembly to rotate the cell. Used to maneuver the InSb sample into position and make the quartz microscope slide horizontal during experiments.
5. A CCD camera (Sony) to view the molten drop, with a lamp at the opposite end of the furnace to illuminate the drop. The camera was connected to a monitor and a computer.
6. A computer equipped with an image acquisition card.
7. A gas supply system consisting of cylinders of the desired gas mixtures, an Oxysorb unit, copper tubing with Teflon fittings connected to the experiment cell, and pressure regulators to measure and control the pressure at the inlet and outlet.
8. An oxygen analyzer to measure the oxygen concentration in the outlet gas. This analyzer included a rotameter to measure the flow rate of the gas in standard cubic feet per hour (scfh).

Figure 3.1 shows a diagram of the furnace with the quartz experiment cell and its connecting tubing.

3.3. Description of components

3.3.1. Split-tube furnace

The split-tube furnace had three zones with eighteen silicon carbide heating rods, nine each on the top and the bottom. Each zone had its own temperature controller (Wahl Instruments Inc.) coupled with silicon-controlled rectifiers (Eurotherm Inc.). Optical-quality fused-silica discs (Chemglass Inc.) were used to cover the large openings on the two ends of the furnace to reduce heat loss and to provide an inside view of the sample to the external CCD camera. The quartz tube connected to the experiment cell passed through holes in these discs, which were 10.6-cm in diameter and 0.63-cm thick.

⁵ "Quartz" is the term commonly used to describe fused silica, i.e. glass made from relatively pure silica. The terms "quartz" and "fused silica" are used interchangeably here, as is common practice.

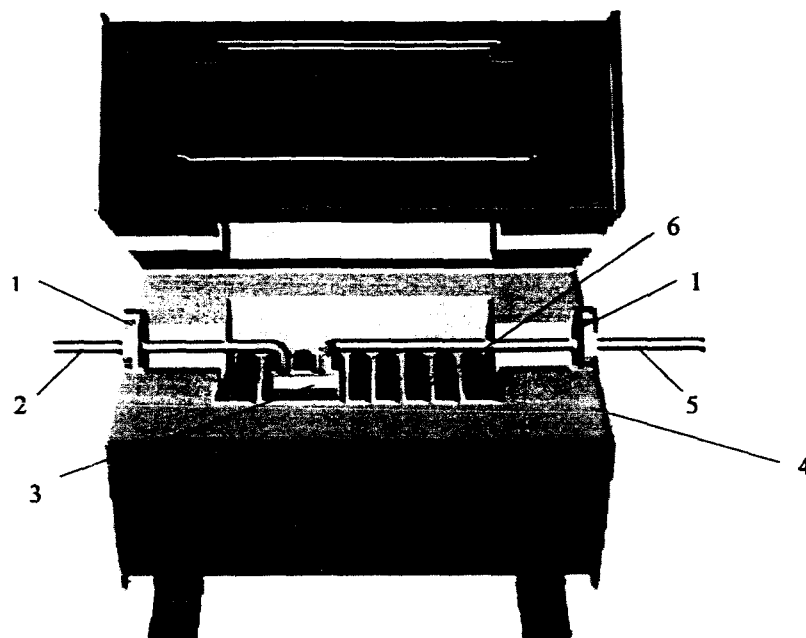


Figure 3.1. Pictorial representation of the furnace. 1. Optical quality fused silica disc. 2. Quartz inlet tube for the cell. 3. Chamber containing the fused silica substrate. 4. Refractory brick insulation. 5. Quartz outlet tube for the cell. 6. Silicon carbide heating elements.

3.3.2. Quartz cell

The experiment cell consisted of an inlet tube, a cylindrical chamber containing the substrate plate, and the outlet tube. The inlet and outlet tubes were 8-mm ID X 10-mm OD. The substrate plate, which was basically a microscopic slide (25 mm X 45 mm), was fused inside a 26-mm ID glass cylinder with optical quality glass windows on both ends. This cylinder with the fused substrate plate is called the chamber. A pictorial representation of the cell is shown in Figure 3.2.

3.3.3. Gas system

To maintain a continuous flow of gas there were gas cylinders, pressure regulators, copper tubes, Teflon fittings, and an Oxisorb unit to remove residual oxygen and water vapor from the gas. Forming gas ($\text{Ar} + 10\%\text{H}_2$) was used for 1 day during preheating the sample and purging the system. Scientific-grade helium was used for the experiments. Forming gas was used for preheating to reduce any oxide present on the sample's surface and, additionally, it is less expensive than scientific-grade helium. A 0.64-cm OD copper tube connected the pressure regulator of the gas cylinder to the quartz inlet tube of the cell. Teflon and stainless steel compression fittings were used for connections and brass swivel fittings were used to facilitate the rotation of the cell. The flow rate of the gas was controlled both by the pressure regulators and by ball valves.

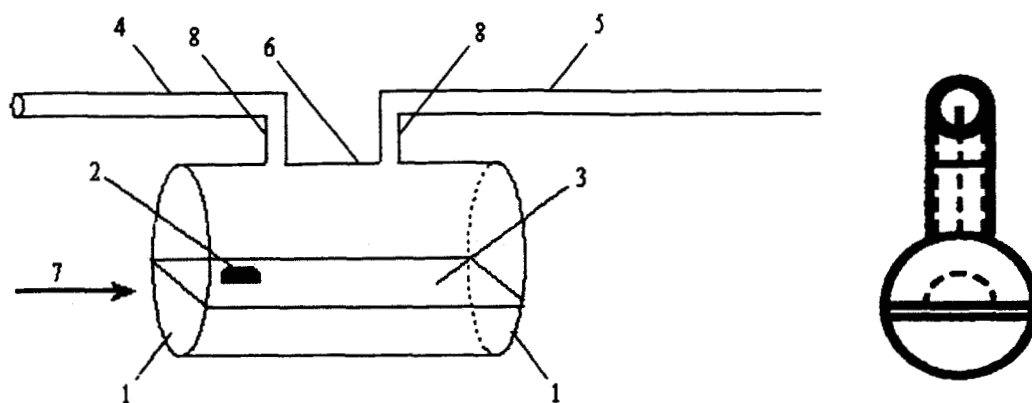


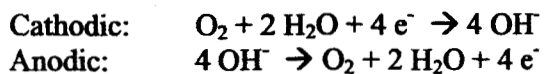
Figure 3.2. Quartz cell. Ground and polished optical-quality fused silica discs (30-mm ID x 32-mm OD). 2. InSb sessile drop. 3. Fused-silica microscope slide (45-mm x 25-mm). 4. Fused silica inlet gas tube (8-mm ID, 10-mm OD). 5. Fused silica outlet gas tube (8-mm ID, 10-mm OD). 6. Fused silica cylinder (26-mm ID). 7. View from the CCD video camera. 8. Risers for inlet and outlet gas tubes (15-mm long).

3.3.4. Oxygen analyzer

The oxygen concentration was measured at the outlet by using a non-depleting coulometric oxygen analyzer (Delta-F Co.). Figure 3.3 shows a photograph of the analyzer. Figure 3.4 shows a diagram of its construction. Its operating range and sensitivity were specified as:

Pressure	-5 to +5 psig
Temperature	5 to 50°C
Flow rate of gas	1 to 5 scfh
Sensitivity	0.01 to 10 ppm of oxygen

In the operation of this analyzer, sample gas diffuses through a diffusion barrier to the cathode, which is in contact with an electrolyte solution [1]. Oxygen is reduced at this electrode to hydroxyl ions. Assisted by a potassium hydroxide electrolyte, the ions migrate to the anode, where they are oxidized back to oxygen. The chemical reactions at the electrodes are:



The electric current produced is proportional to the number of oxygen molecules reduced at the cathode. Because there is no membrane attached to the diffusion barrier, the response is rapid.



Figure 3.3. Photograph of the Delta-F oxygen analyzer.

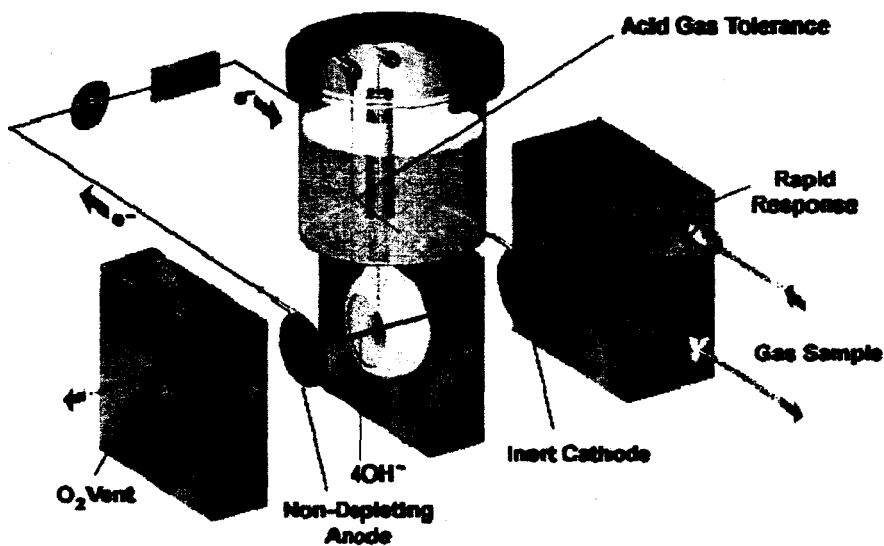


Figure 3.4. Schematic diagram the Delta-F oxygen analyzer [1].

3.4. Experimental methods

The basic principle of studying a sessile drop of molten InSb remained the same, although there were numerous changes made in the experimental techniques, apparatus and analysis methods. It was observed that cleanliness was one of the most important factors in obtaining accurate results, so some changes were made in the experimental methods. Extreme care was taken to

achieve cleanliness. The methods used here are described below, including the changes that were made from the previous methods and the reasons for these changes.

3.4.1. Changes in the apparatus

In the previous experiments, we were unable to achieve sufficiently low oxygen concentrations. Consequently, all unnecessary fittings were removed from the gas flow system because each fitting represents an opportunity for a leak of air into the system. The Teflon compression fittings were replaced with new ones because Teflon slowly deforms when stressed. The Oxisorb unit was replaced with a new one. To provide more precise control of pressures from 3 to 4 psig, the 0-60 psig feed gas regulator was changed to one with a range of 0-30 psig.

The quartz cell was frequently replaced with a new one, with no more than four experiments conducted using each. This replacement was done because of concern over accumulated damage to the surface of the quartz plate due to sticking by the solidified drops. The length of the substrate plate and chamber was decreased from 75 mm to 45 mm because the extra length was not needed and had the disadvantage of increasing the stress on the plate, sometimes even resulting in cracks. The diameter of the glass cylinder forming the chamber was decreased from 30 mm to 26 mm so that the 25-mm wide plate rested on a chord positioned at a higher level than before, thereby providing a better view of the drop. The rear end of the substrate plate was not allowed to touch the back chamber window, thereby greatly facilitating gas exchange with the portion of the chamber beneath the plate. A diagram of the resulting chamber is shown in Figure 3.5.

Previously, a VCR was used with the CCD camera to record sessile-drop images, some of which were grabbed later for use in analysis. The VCR was replaced by a computer with an image acquisition card (National Instruments Inc.) in it. The resolution of these digital images was far better than those obtained using the analog video tapes.

3.4.2. Experimental procedure

The step by step procedure was as follows:

- Cell preparation
 - Cleaning
 - Preheating (1100°C for 24 h)
 - Purging with forming gas during preheating.
- Sample cleaning
- Introduction of sample into the cell
- Attachment of the cell to the gas flow system
- Preheating the sample for 24 h at 400°C while purging with forming gas
- Varying the furnace temperature to aid in removal of gas from beneath the plate
- Melting of the sample after the oxygen concentration became constant
- Vibrating and tilting the cell to position the molten InSb, followed by adjusting the plate to horizontal
- Capture images using the CCD camera connected to a computer equipped with an image acquisition card
- Detailed analysis of images

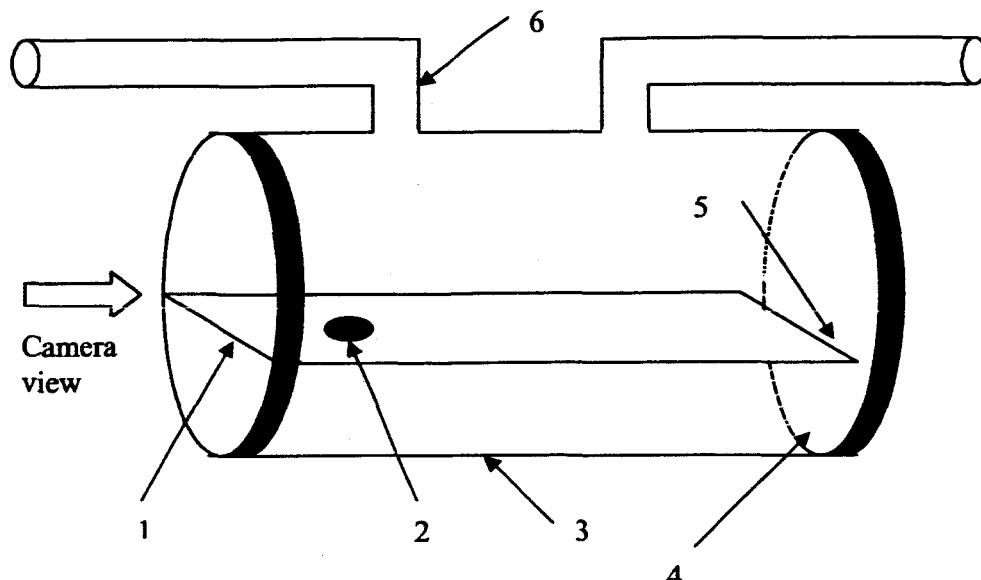


Figure 3.5. Fused silica Cell. 1. substrate plate (25x45-mm microscopic slide), 2. pure InSb sample, 3. glass cylinder (26x45 mm), 4. optical quality fused silica plate (26-mm diameter), 5. ~1 mm. gap, 6. riser for inlet and outlet gas tubes (12 mm)

3.4.2.1. Cell preparation

The quartz cell was soaked in aqua regia⁶ for about 24 h, followed by thorough rinsing with de-ionized water, acetone and methanol. The cell was allowed to dry completely under ambient conditions before introduction into the furnace for preheating.

The cell was inserted into the furnace with forming gas flowing at 1 SCFH. The temperature was slowly increased for 30 min and maintained at 1100°C for 24 h while the forming gas continued to flow. There were three reasons for this prolonged purging. The first was to remove chemisorbed water from the substrate plate, because the resulting -OH is known to affect the contact angle of molten metals on silica [2]. The second reason for purging with forming gas was to reduce any indium or antimony oxide. The third reason was to remove gas from beneath the plate. To assist in the latter, the furnace temperature settings were from time-to-time suddenly decreased and then increased. After 24 h of treatment the furnace was turned off with the forming gas still flowing until the temperature fell to about 60°C-80°C. The cell at this time was ready for sample introduction.

Changes in cell preparation from previous procedure

- Prolonged heating at 1100°C to minimize -OH on plate surface
- Occasional step changes of ~600°C in temperature over a period of 6-7 hours.

⁶ 1:3 ratio by volume of 67% HNO₃ and 37% HCl

3.4.2.2. Sample cleaning

Pure zone-refined InSb was donated by Firebird Semiconductors. A small piece was soaked in diluted HCl⁷ for about 12 h followed by rinsing with methanol in an ultrasonic bath, in order to remove surface impurities. The sample was removed from the bath and wiped using delicate task wipers (Kimwipes Inc.), and wrapped and stored in a new Petri dish for the short time before it was introduced into the cleaned quartz cell. Extreme care was taken to keep the sample clean and dry. The above cleaning was performed just after the cell had cooled from the preheating treatment in order to avoid unnecessary exposure of the clean sample to ambient air.

3.4.2.3. Introduction of the sample and preheating at 400°C

After the sample was cleaned and the furnace had cooled to 60-80°C, the sample was introduced into the cell as quickly as possible to avoid minimum intrusion of air. A temperature of 60-80°C was hoped to be sufficient to avoid absorption of water vapor accompanying the air during introduction of the InSb sample. As soon as the sample had been introduced, the cell was reconnected to the gas supply system and forming gas flowed through it at 8-10 psig to remove the air that had intruded while introducing the sample. After flushing for 5-10 min, the furnace temperature was increased to about 200°C and held there for 30 min. The flow rate of forming gas was kept at about 5 SCFH. The furnace temperature was increased to 400°C and held there for 12 h, during which the furnace temperature setting was suddenly raised and lowered. After 12 h, the oxygen analyzer was turned on. It was important to turn the oxygen analyzer on only after the oxygen concentration had fallen, because the manufacturer recommended that it not be exposed to a gas having more than 25% oxygen [1]. A typical oxygen analyzer response is shown in Figure 3.6.

Change from previous procedure

Quick introduction of the sample into a warm cell.

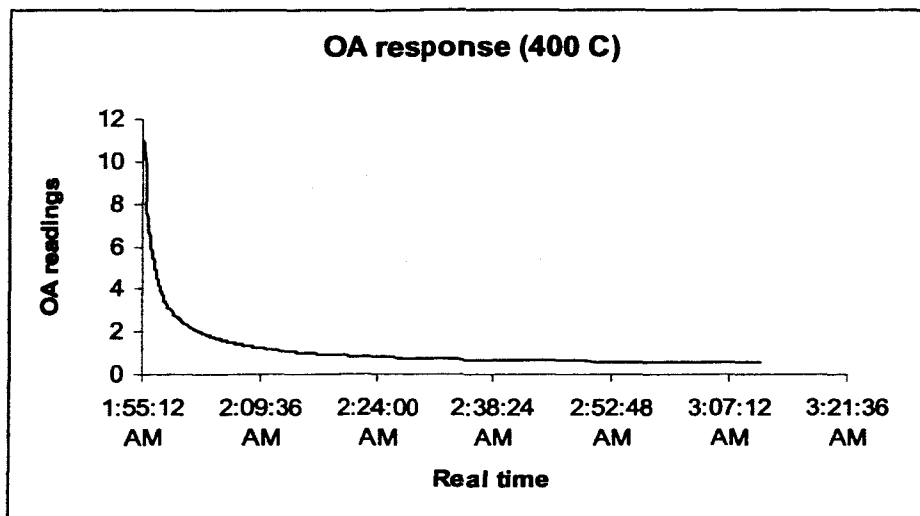


Figure 3.6. Oxygen analyzer reading after purging with forming gas for 12 h at 400°C.

⁷ 1:3 37% HCl and de-ionized water

3.4.2.4. Melting the sample

After 12 h of heating and purging at 400°C, the gas supply was switched from forming gas to scientific-grade helium, which flowed for another 12 h. This was followed by raising the furnace temperature in increments of 50°C every 30 min until it reached 600°C. (The melting point of pure InSb is 536°C [3].) The portion of the cell just protruding from the furnace was slowly tapped by hand to avoid pinning of the drop, i.e. sticking of the contact line to the surface of the plate. The cell was left under these conditions until the oxygen concentration no longer decreased, approximately another 48 h. The oxygen concentration at this point in all the experiments was 0.08-0.09 ppm.

After the above treatment, the drop had assumed what appeared to be an axisymmetric shape. It rolled freely when the substrate plate was tilted as slowly as 0.23 rpm by employing the motor-gear assembly. The drop was then brought into the middle of the plate using the cell rotating assembly. It was illuminated from the exit end of the furnace using a bare 100 watt bulb. A silhouette image of the drop was obtained at the camera end by placing an IR filter just in front of the camera lens. An image of the drop was now available to be grabbed by the CCD camera connected to the computer. LabView software on the computer was used with the frame-grabber board to save high resolution digital pictures directly from the camera. One such digital picture is shown in Figure 3.7.

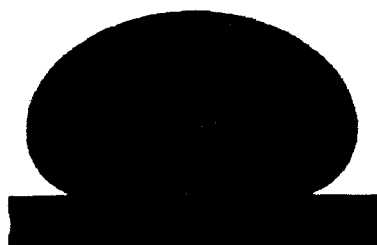


Figure 3.7. Digital image of a silhouette of an InSb drop.

Changes from previous procedure

- Purged with helium for 48 h
- Computer used to grab drop images directly from the CCD camera input
- Oxygen concentrations as low as 0.08 ppm could be achieved compared to 0.2-0.3 ppm in previous experiments.

3.4.3. Data analysis

Extracting contact angles from the sessile drop images consisted of the following four steps. These are shown diagrammatically in Figure 3.8.

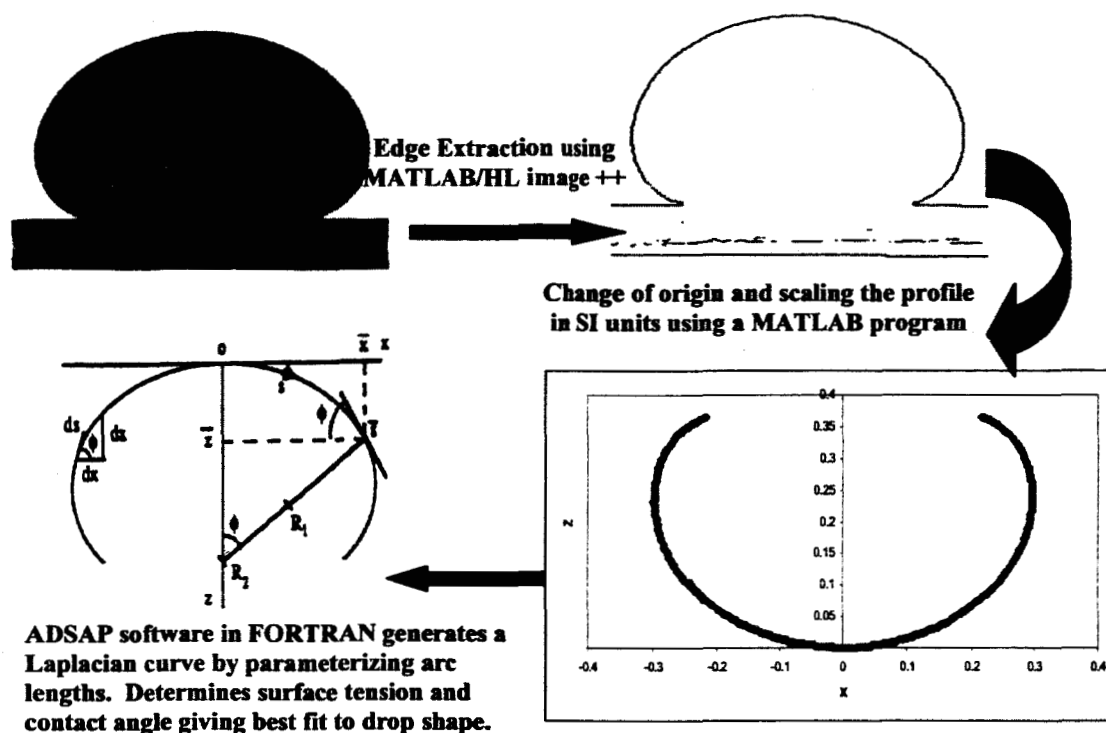


Figure 3.8. Steps in converting the drop image to values of surface tension and contact angle.

3.4.3.1. Edge extraction

The digital images of the drop were processed with the MATLAB function "batchscript," which uses the Prewitt edge operator [4] to return a binary image of the edge of the drop. This method finds edges using the Prewitt approximation to the derivative, and returns edges at those points where the gradient of the image is a maximum.

3.4.3.2. Drop profile detection

The edge thus obtained was in binary format. This edge picture was opened using paint software. The region of interest was selected and saved in a 256-bit color image file, as illustrated in Figure 3.9. The plate edge was removed using the "fill with color" toolbar in paint to convert the flat pixels to black, so that only the drop outline remained. (As shown in Figure 3.10, the horizontal plate could easily be seen by magnifying the edge image to 8 times.)

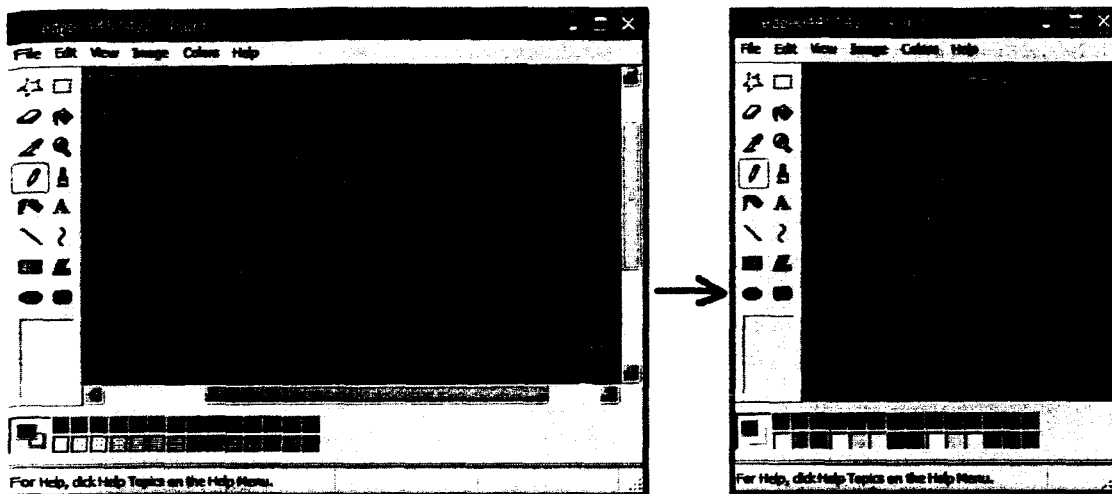


Figure 3.9. Selection of the required region of interest and saving in the 256-bit format

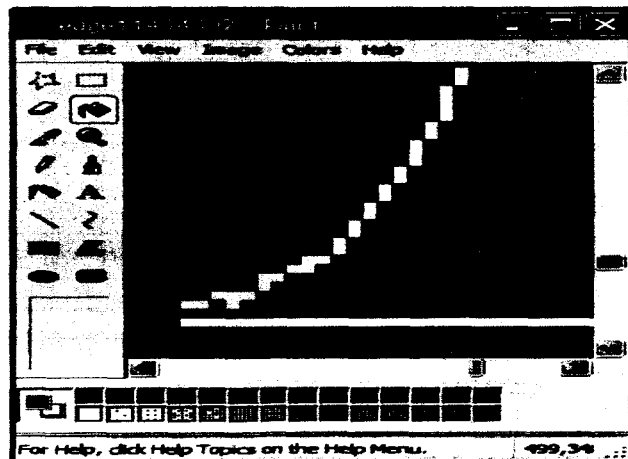


Figure 3.10. Magnified image to aid in blackening out the horizontal plate's pixels.

3.4.3.2. Determination of the coordinates, contact points and height of the drop

The data for the cropped region of interest were now loaded into MATLAB, which returned the coordinates in SI units. The calibration was done using a frame from the CCD camera focused on a sheet of graph paper inside the furnace that was moved until the image was sharp. The position of the graph sheet should have exactly matched the position of the drop because the camera focus had not been changed. The corresponding number of pixels in 1 cm length of the graph was the scaling factor required to convert pixels into SI coordinates. The number of pixels was calculated using the measurement tool of HL image ++ 98 software (Western Vision Software), as shown in Figure 3.11.

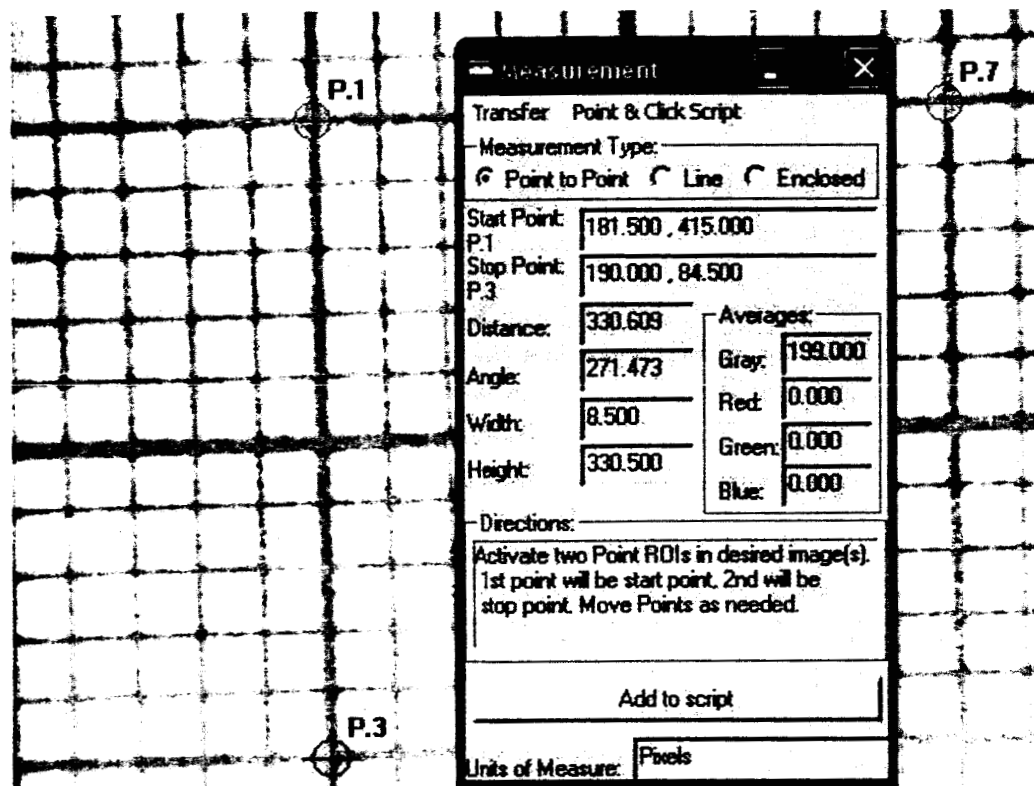


Figure 3.11. Conversion of pixels into SI units. Here, 1cm ~330 pixels.

The MATLAB program pixcoord determined all the necessary parameters and no manual input was required. This program was also used to calculate the density difference between molten InSb [3] and the surrounding helium gas, assuming the gas to be ideal. The governing equations are:

$$\rho_{\text{InSb}} (\text{g/cm}^3) = 7.111 - (0.0006542)(t + 273) \quad (3.1)$$

$$\rho_{\text{He}} (\text{g/cm}^3) = \frac{(0.00018)(273)}{t + 273} \quad (3.2)$$

$$\Delta\rho (\text{g/cm}^3) = \rho_{\text{InSb}} - \rho_{\text{He}} \quad (3.3)$$

The output was a text file of drop coordinates, which were the required input for ADSAP [19]. ADSAP utilizes Fortran code to generate a Laplacian curve by parameterizing arc lengths and determines the surface tension and contact angle giving the best fit to the experimental drop coordinates.

3.4.3.4. Problems with previous method of analysis

The previous method used a C program called "boundary," which required the following inputs to calculate the drop's edge coordinates and convert these to SI units (See Figure 3.12):

- Left contact point (x_1, y_1)
- Right contact point (x_2, y_2)
- Height of the drop (y_0)

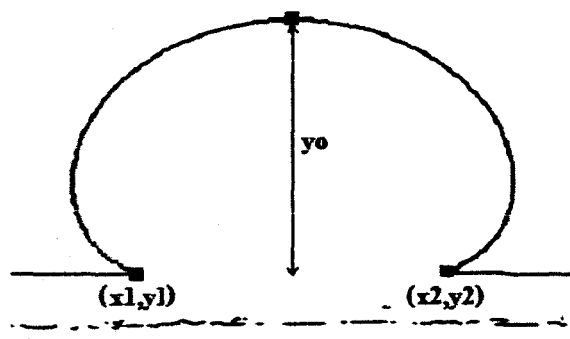


Figure 3.12. Three-phase points of contact and the apex of the drop.

These five inputs required manual observations, which tend to differ from user to user and experiment to experiment, and are, therefore, not very dependable. As illustrated in Figures 3.13-15, the contact angle given by ADSAP was highly dependent on the y-coordinates of the contact points (y_1, y_2) , and less dependent on the abscissas (x_1, x_2) and the maximum height (y_0) of the drop.

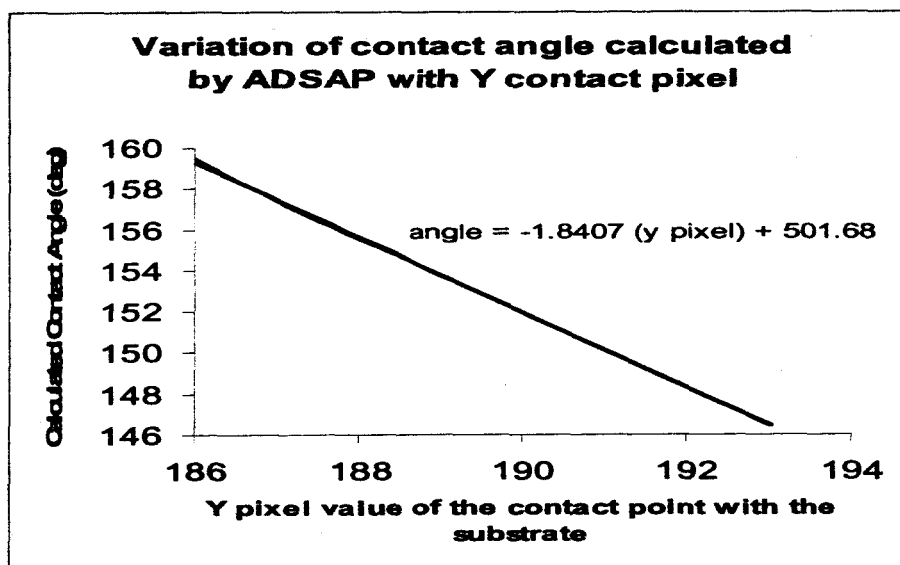


Figure 3.13. Influence of contact point y-pixel value on contact angle calculated by ADSAP.

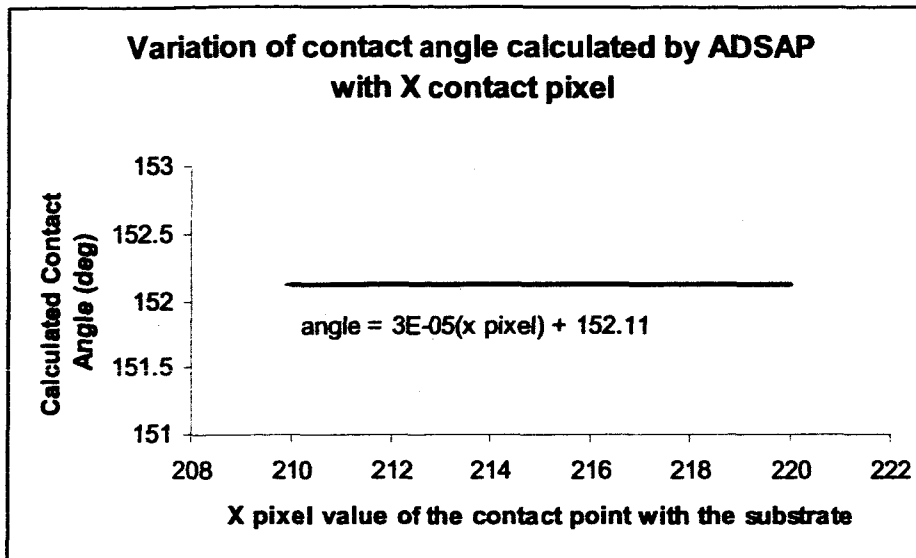


Figure 3.14. Influence of contact point x-pixel value on contact angle calculated by ADSAP.

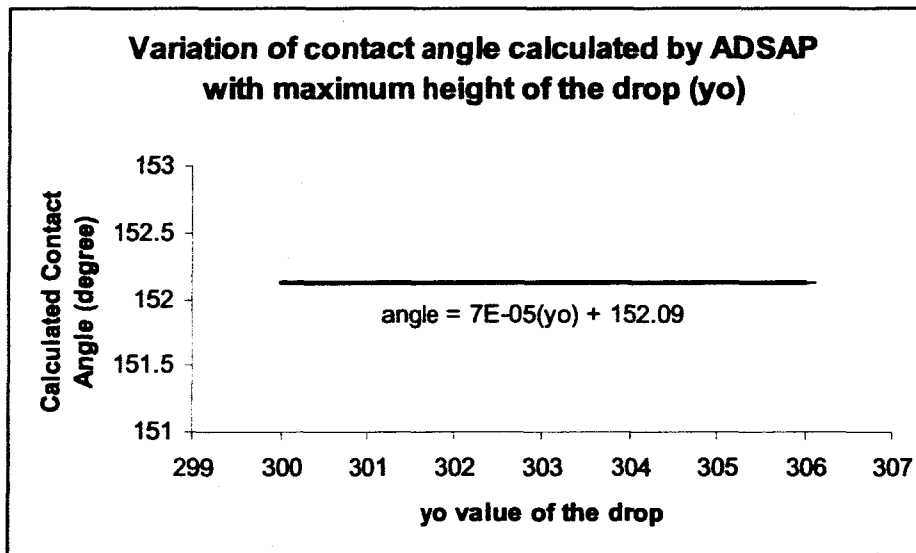


Figure 3.15. Influence of maximum drop height yo on contact angle calculated by ADSAP.

Thus, the accuracy of the ADSAP result is highly dependent on the accurate detection of contact points, which with manual observation cannot be relied upon. Therefore, a MATLAB code was written that determines the contact points and the maximum height of the drop directly from the digital image of the drop edge.

Changes from previous procedure

- Automatic detection of contact points and height of the drop using the MATLAB program pixcoord.
- Only the useful part of the image was used and was magnified 8 times to remove the substrate line using a paint tool.

3.4.4. Contact angle determination using a polynomial fit near the contact point

The currently available implementations of ADSAP are not applicable to all situations, e.g., in the presence of an electric field and for non-axisymmetric drops [5]. An alternative scheme is to fit a polynomial to the drop shape near the contact point where the three interfaces meet, and then differentiate the polynomial to get the contact-point slope, which is the contact angle. An associated problem is to decide the number of pixels to be fit and the order of the polynomial. It is desired that the contact angle results should not be too sensitive to the number of pixels taken (P) and the order of the polynomial (O). Therefore, various drop profiles were fitted with varying orders and number of pixels to examine the accuracy and stability of the results. A first-order polynomial is very sensitive to the number of pixels and is, therefore, not suitable [5]. With higher order polynomials the calculated contact angle increases with increasing number of pixels P until P has little effect on the contact angle, followed by a decrease in the results with further increase in P (Figure 3.17). The correlation coefficient was selected as a good statistical criterion because its behavior is similar to the sensitivity of the contact angle [5]. The square of the correlation coefficient R^2 is defined as:

$$R^2 = \frac{\sum_i (Y_{\text{polynomial}} - \hat{Y}_{\text{profile}})_i^2}{\sum_i (Y_{\text{profile}} - \hat{Y}_{\text{profile}})_i^2} \quad (3.4)$$

Basically, it is the fraction of the standard deviation of experimental measurements that is explained by a correlation. Thus, in the present case $R^2 = 1$ would represent all pixels for the drop profile falling exactly on the polynomial fit.

Another statistical tool which can be used to optimize fitting to the drop profile is the standard error, which is defined here as:

$$S = \sqrt{\frac{\sum_j^P (Y_{\text{polynomial}} - Y_{\text{profile}})_j^2}{P - (O + 1)}} \quad (3.5)$$

The standard error was found to be low when the number of pixels, P, was small for each order of polynomial O (Figure 3.18). However, the minimum standard error was almost equal (i.e. ~ 0.8) for all orders of polynomials. The correlation coefficient and the standard error criteria can be used to determine the optimum number of pixels and order of polynomial. By experimentation, it was concluded that a third-order polynomial fit over a curve length of about 0.5 mm is best [5].

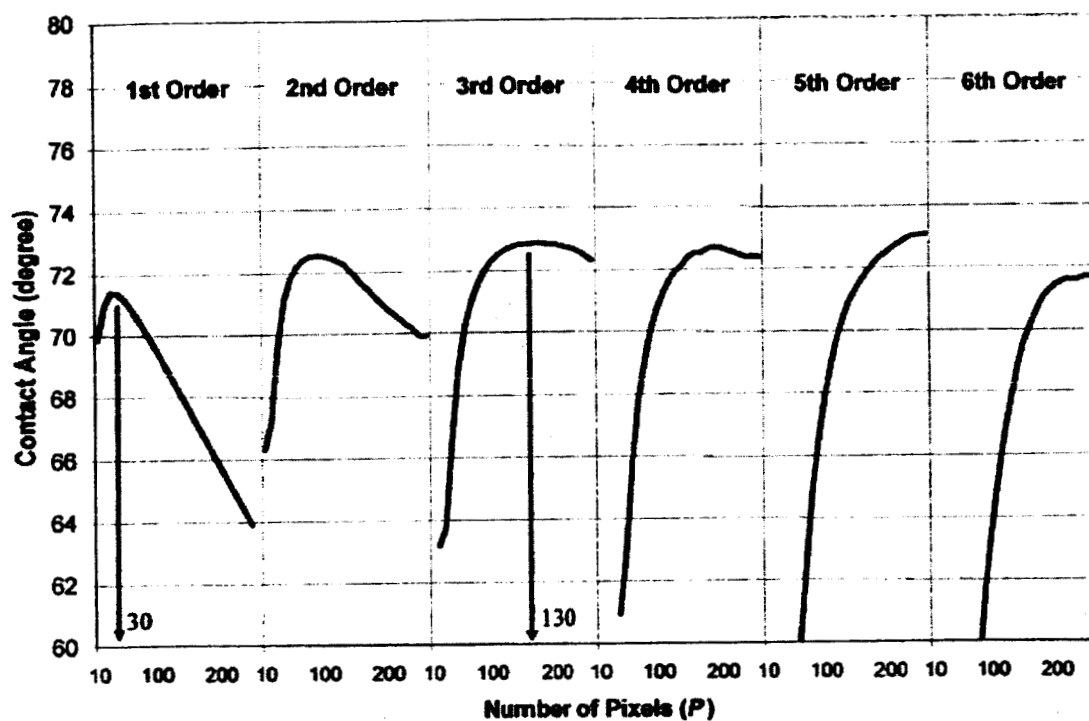


Figure 3.16. Average contact angles for different orders of polynomial fit, versus the number of pixels [5].

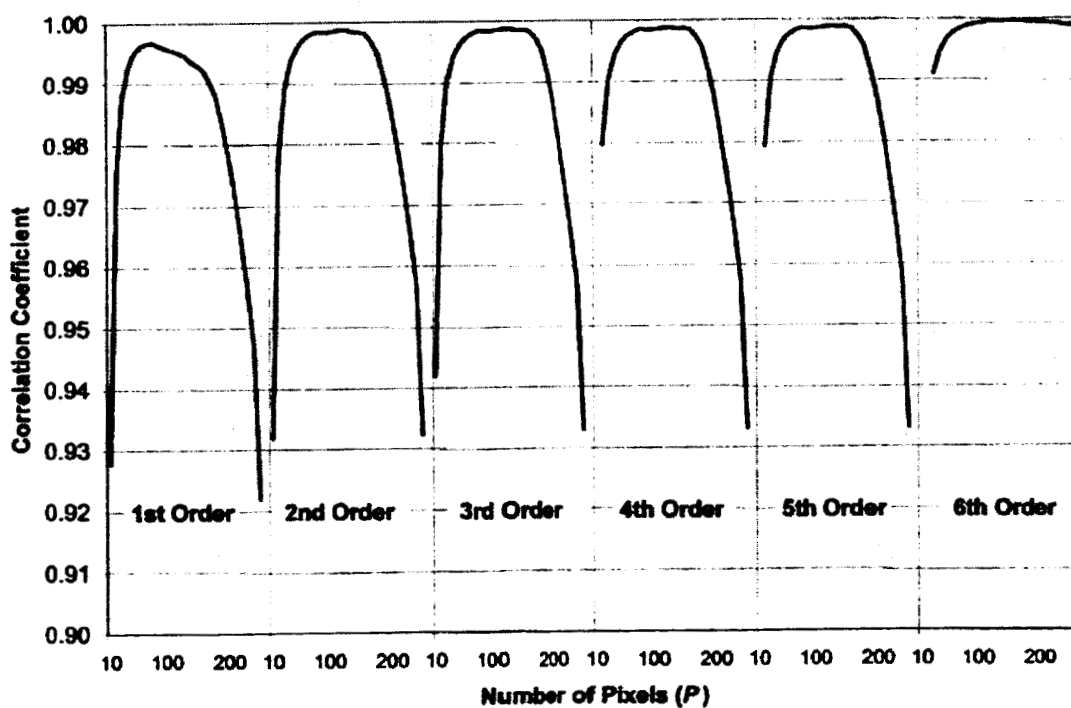


Figure 3.17. Square of the correlation coefficient (R^2) for different orders of polynomial fit, versus the number of pixels [17].

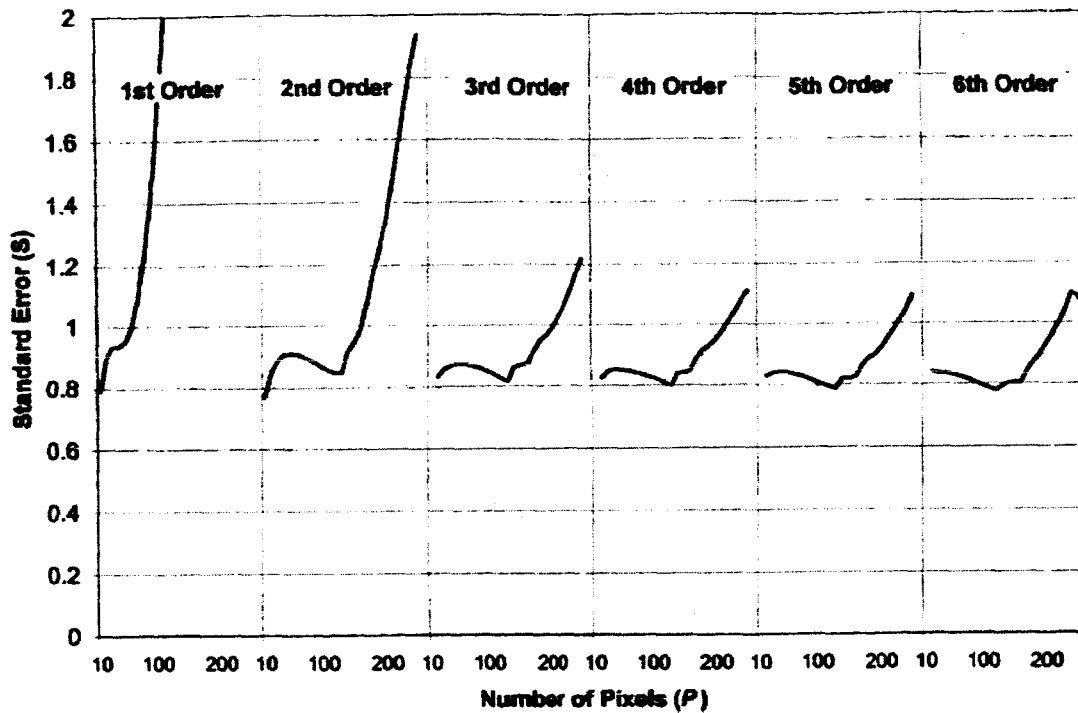


Figure 3.18. Standard error (S) for several polynomials for different orders of polynomial fit, versus the number of pixels [5].

3.4.4.1. Lagrangian polynomial fitting

This kind of interpolation uses the concept of divided differences when the x-values are not evenly spaced. Consider, for example, the data table below:

x	$f(x)$
x_1	f_1
x_2	f_2
x_3	f_3
x_4	f_4

If Δx is not uniform, then a cubic polynomial can be passed through these 4 data pairs. The Lagrangian form of this is given in [6] as:

$$P(x) = \frac{(x-x_2)(x-x_3)(x-x_4)}{(x_1-x_2)(x_1-x_3)(x_1-x_4)} f_1 + \frac{(x-x_1)(x-x_3)(x-x_4)}{(x_2-x_1)(x_2-x_3)(x_2-x_4)} f_2 + \frac{(x-x_1)(x-x_2)(x-x_4)}{(x_3-x_1)(x_3-x_2)(x_3-x_4)} f_3 + \frac{(x-x_1)(x-x_2)(x-x_3)}{(x_4-x_1)(x_4-x_2)(x_4-x_3)} f_4 \quad (3.4)$$

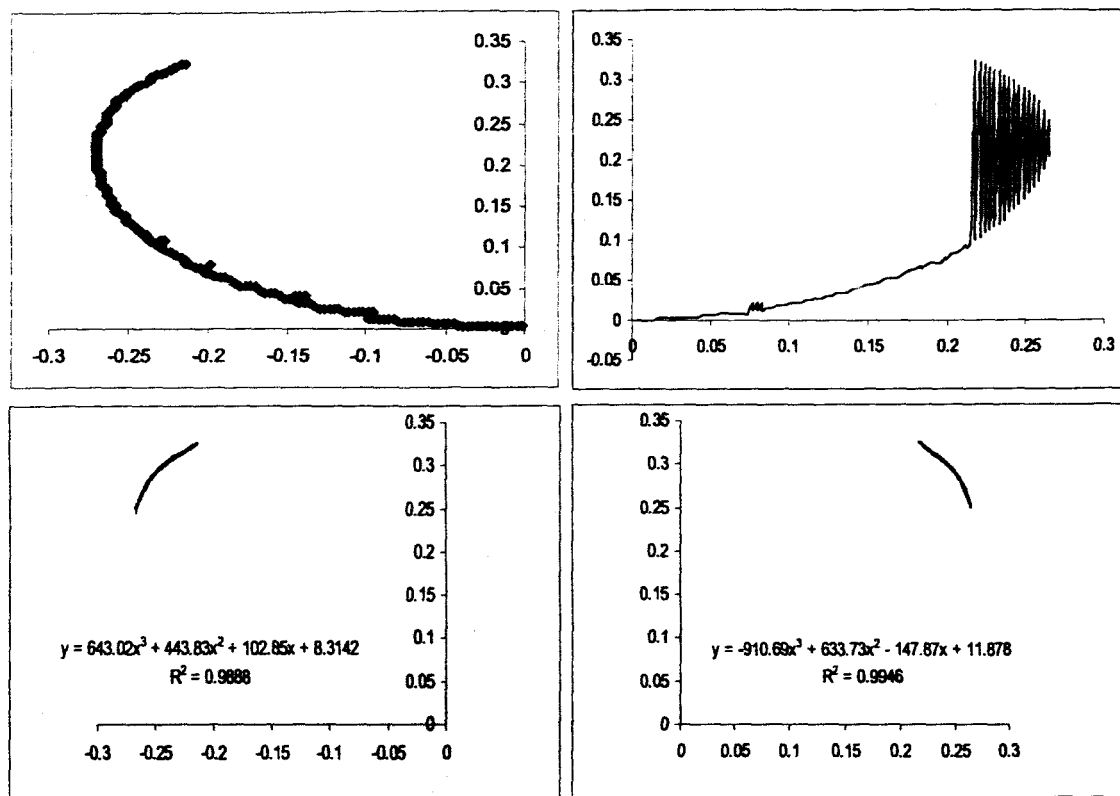


Figure 3.19. Lagrangian polynomial fitting: 0.5mm section near the contact point

References

1. Delta F Oxygen and Moisture Analyzers: <http://www.delta-f.com/senstech.html> (Delta F Corporation, Woburn, MA).
2. R. Sangiorgi et al., J. Am. Ceram. Soc., 171, 742-748 (1988).
3. X. Chen, Q. Wang, K. Lu, "Temperature and Time Dependence of the Density of molten Indium Antimonide measured by an Improved Archimedean Method," J. Phys.: Condensed Matter, 11, p.10335 (1999).
4. A.C. Bovik, Handbook of Image and Video Processing, Academic Press, San Diego, CA (2000).
5. A. Bateni et al., Colloids and surfaces A, Physiochem Eng. Aspects, 219, 215-231 (2003).
6. C.F. Gerald and P.O. Wheatley, Applied Numerical Analysis, 6th edition (Pearson Higher Education, 1998) p. 47

4. RECENT RESULTS ON HIGH-PURITY InSb

As discussed in section 3.4.3.4 and shown in Figure 3.13, the contact angle given by ADSAP is highly dependant on the y coordinate of the contact point. The slightest error in the determination of contact point can cause a large error in the calculated contact angle. In using the Laplace equation of capillarity to determine the contact angle and surface tension giving the best fit to the drop coordinates, ADSAP assumes that the drop is perfectly axisymmetric. Experimentally, however, this assumption is not always true. In addition, several factors can add to uncertainty near the contact point and, thereby, errors in the result. These factors include reflection from the substrate plate, reflections from the shiny metallic drop, and a non-axisymmetric shape may add to noise near the contact point. Therefore, an alternative scheme was adopted to calculate contact angle that uses a polynomial to fit the drop profile near the contact point. This technique can be used to find the contact angles on both the sides of the drop, which often differ by two to three degrees. It also eliminates the high dependence of contact angle on the contact point when using ADSAP. It is reported that the higher the order of the polynomial (up to 10) the better the resulting contact angle agrees with that from ADSAP [1].

4.1. Polynomial technique to determine contact angle

4.1.1. Fitting function

The coordinates (x,y) of the drop's edge were extracted by the "pixcoord" program in MATLAB. There are two different forms of the polynomial function that can be used for fitting -- either $y = f(x)$ or $x = f(y)$. In both cases, the contact angle is found by differentiating the polynomial to obtain the slope at the contact point. It has been reported that when the contact angle is near 90° , the form $y = f(x)$ yields more accurate results, whereas if the contact angle is near 180° the form $x = f(y)$ yields better results [1]. This is verified for one of the experiments, as shown in Figure 4.1. The correlation coefficient R is consistently closer to 1 for a polynomial fit of the form $x = f(y)$ than for $y = f(x)$. Figures 4.2 and 4.3 show the drop profiles using $y = f(x)$ and $x = f(y)$.

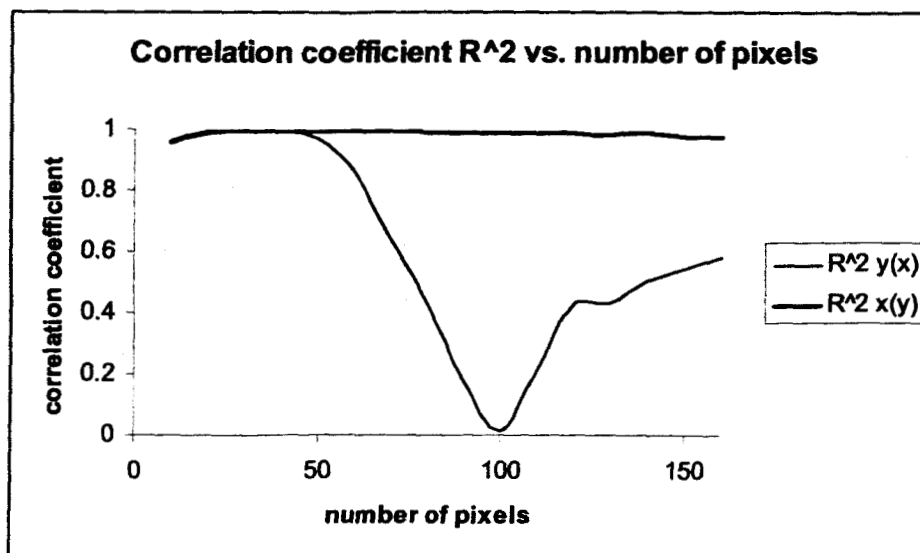


Figure 4.1. Correlation coefficient squared vs. the number of pixels used to generate $x=f(y)$ and $y=f(x)$.

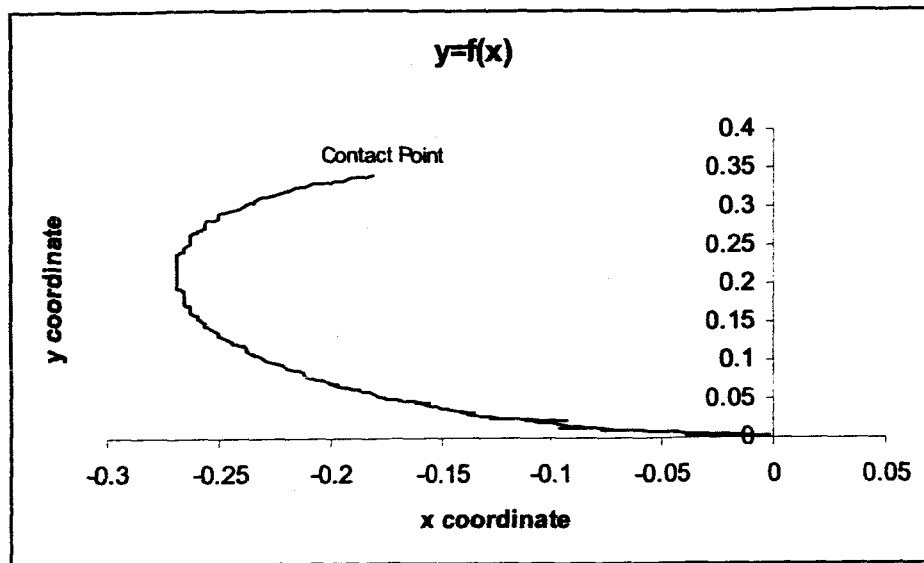


Figure 4.2. Drop profile for $y=f(x)$. Contact Angle = $\arctan(dy/dx)_{\text{contact point}}$

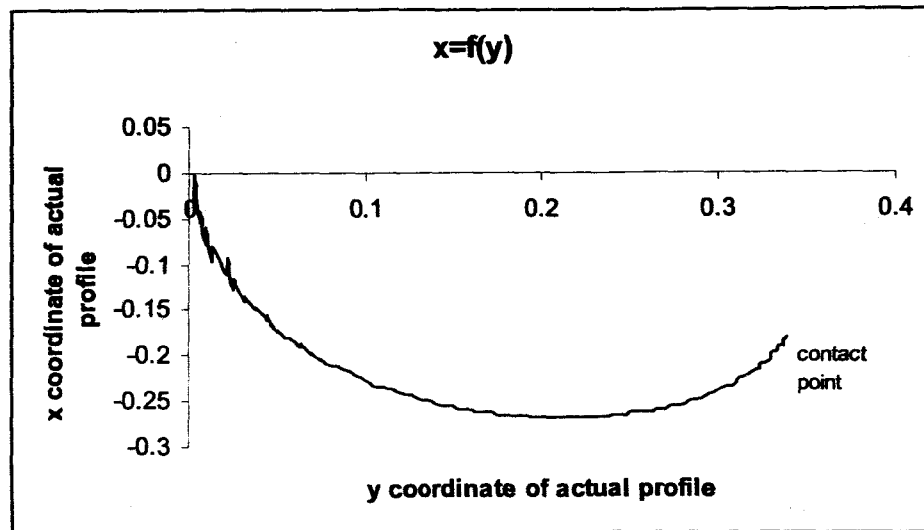


Figure 4.3. Drop profile as $x=f(y)$. Contact angle = $180^\circ - \arctan(dx/dy)_{\text{contact point}}$

4.1.2. Order of polynomial and the number of pixels used

In section 3.4.3.4 it was indicated that a third-order polynomial yields accurate results when pixels near the contact point are used for fitting the drop profile. The drop size and the pixel size used by *Bateni et al.* [2] differ from those used here. Therefore, the optimal number of pixels for fitting the drop profile was determined empirically by plotting the square of the correlation coefficient R^2 versus the number of pixels near the contact point. Figure 4.4 shows that the optimum number of pixels is about 45 for a third-order polynomial. Compare this with Figure 3.17.

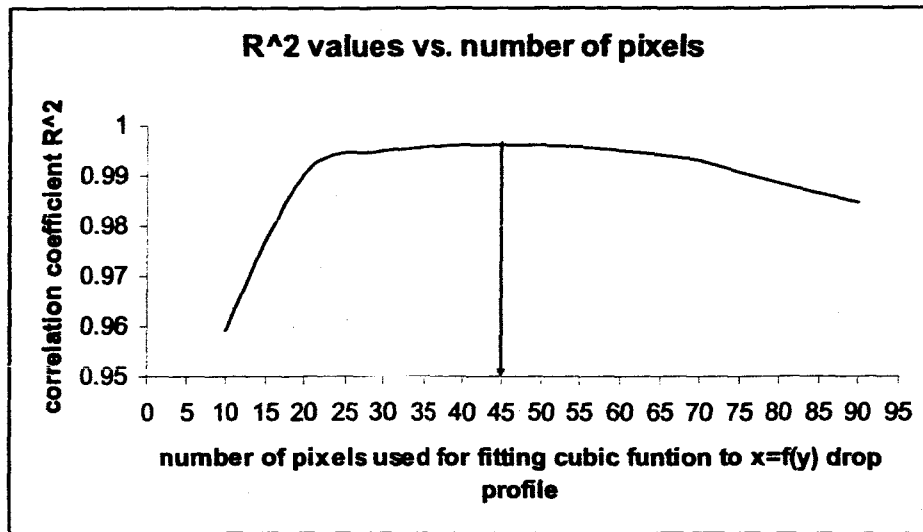


Figure 4.4. The square of the correlation coefficient versus the number of pixels near the contact point, from fitting a third-order polynomial to the drop profile.

4.1.3. Substrate plate tilt correction

The contact angle is the inverse tangent of the slope at the contact point found using the fitted polynomial, i.e.:

$$\text{Contact Angle: } \theta = 180^\circ - \tan^{-1}(dx/dy)_{\text{contact point}} \quad (4.1)$$

This equation is valid only if the substrate plate is perfectly horizontal. However, it is quite probable that the plate was tilted so slightly that this could not be observed during the experiment. The tilt angle of the plate should be subtracted from the angle obtained from equation 4.1 above. The tilt angle was determined using the measurement toolbar of HL image software, as shown in Figure 4.5.

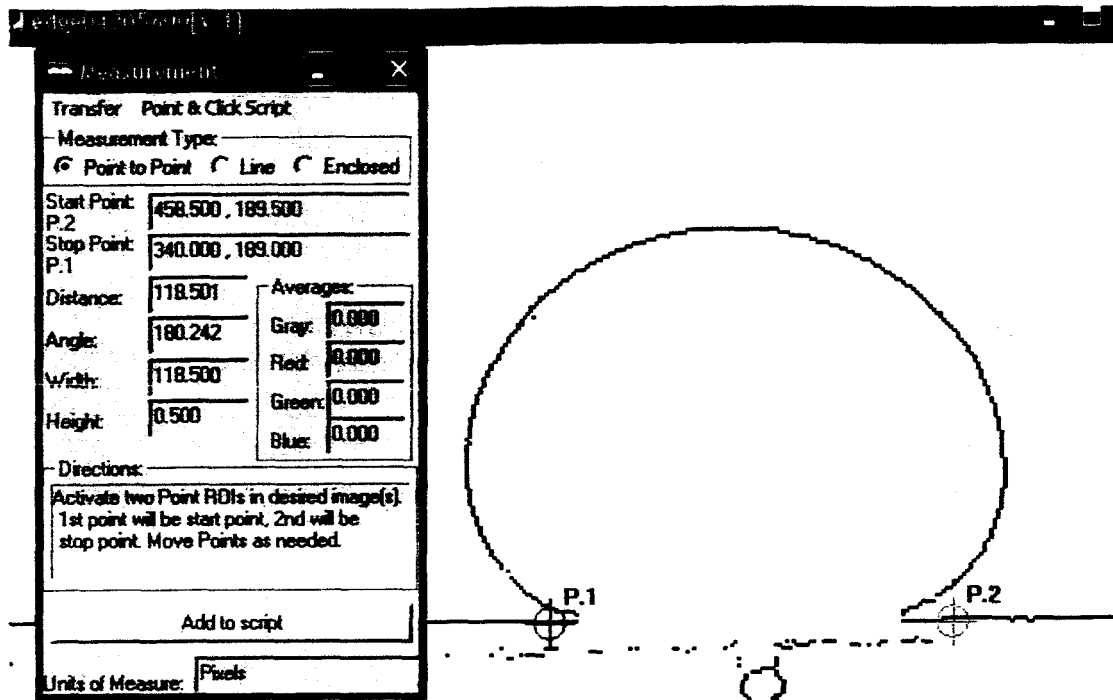


Figure 4.5. Measurement toolbar of HL image software used to determine the tilt angle β . Here, $\beta \sim 0.24^\circ$.

So, the final equations used to calculate contact angles from the drop profile $x=f(y)$ are:

$$\text{Right Contact Angle: } \theta_r = 270^\circ - \tan^{-1}(dx/dy)_{\text{contact point}} - \beta \quad (4.2)$$

$$\text{Left Contact Angle: } \theta_l = 90^\circ + \tan^{-1}(dx/dy)_{\text{contact point}} + \beta \quad (4.3)$$

See Figure 4.6 for an example. Table 4.1 shows some experimental results.

References

1. O.I. del Rio *et al.*, "Contact angle measurements by axisymmetric drop shape analysis and an automated polynomial fit program," *Physiochem. Eng. Aspects*, 143 (1998) 197-210.
2. A. Bateni *et al.*, "Colloids and surfaces," *Physiochem. Eng. Aspects*, 219 (2003) 215-231.

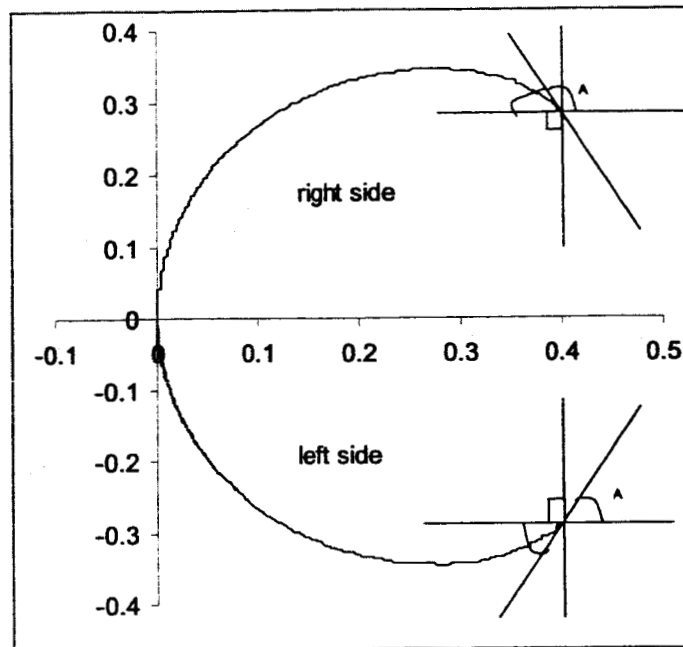


Figure 4.6. Left side and right side contact angles using a third-order polynomial of the form $x = f(y)$.

Table 4.1. Some experimental results.

Experiment	Gas used	Substrate tilt (β)	Left Contact Angle	Right Contact Angle	ADSAP Contact Angle	Surface Tension (N/m)	Image acquisition card used	Oxygen (ppm)
1/dec31a	He	1.5°	142.9°	144.4°	142°	.51	Yes	0.08
2/nov26a	He	0.40°	142.8°	141.8°	142.27°	.48	Yes	0.08
3/oct28a	He	0.43°	139.1°	138.6°	144.32°	.53	Yes	0.08
4/oct13a	He	0.7°	140.1°	139.3°	141.0°	--	Yes	0.08
5/aug20a	Ar+10% H ₂	.1°	144.9°	146.7°	155.67°	.37	No	0.08
6/aug8a	He	0.45°	139.8°	138.3°	144.17°	.38	No	0.08
7/jan6	Ar+10% H ₂	0.24°	155.5°	154°	157.5°	.43	No	0.16
8/dec24	Ar+10% H ₂	0.24°	146.5°	150.5°	157°	.36	No	0.17
9/dec16	Ar+10% H ₂	0.1°	146.5°	147.0°	153°	.46	No	0.29
10/july15	Ar+10% H ₂	.7°	147.6°	146.5°	154.1°	0.38	No	0.68